

Contributions of External Forcing and Internal Climate Variability to Changes in the Summer Surface Air Temperature over East Asia

JINLIN ZHA,^{a,b} CHENG SHEN,^c DEMING ZHAO,^b JINMING FENG,^b ZHONGFENG XU,^b JIAN WU,^a WENXUAN FAN,^a MENG LUO,^d AND LIYA ZHANG^e

^a Key Laboratory of Atmospheric Environment and Processes in the Boundary Layer over the Low-Latitude Plateau Region, Department of Atmospheric Science, Yunnan University, Kunming, China

^b CAS Key Laboratory of Regional Climate and Environment for Temperate East Asia, Institute of Atmospheric Physics, Chinese Academy of Sciences, Beijing, China

^c Regional Climate Group, Department of Earth Sciences, University of Gothenburg, Gothenburg, Sweden

^d Yunnan Climate Center, Kunming, China

^e Shanghai Pudong Meteorological Bureau, Shanghai, China

(Manuscript received 31 July 2021, in final form 5 April 2022)

ABSTRACT: Summer mean (June, July, and August) surface air temperature (SSAT) in East Asia during the period from 1958 to 2001 has shown a warming. However, the relative contributions of external forcing (EF) and internal climate variability (ICV) to the SSAT changes over East Asia remain unclear. In this study, a new approach is applied to estimate the changes in the SSAT determined by the effects of EF and ICV over East Asia during the period from 1958 to 2001. Reanalysis data as well as simulated results from both global atmosphere–ocean coupled model outputs and a regional climate model (RCM) are used for this approach. The observed SSATs over East Asia have undergone a decreasing trend from 1958 to 1972 ($-0.14^{\circ}\text{C decade}^{-1}$, $p < 0.01$) and an increasing trend after 1972 ($0.24^{\circ}\text{C decade}^{-1}$, $p < 0.01$). While these features are not captured by the reanalysis studied here, they are reproduced when the reanalysis output is down-scaled using an RCM. The effects of the EF and the ICV on the SSAT can be separated based on the RCM downscaling simulation. The results show that the SSAT with EF displayed significant warming over most regions of East Asia, whereas the SSAT with ICV mainly exhibited cooling over East Asia. Furthermore, EF mainly influenced the decadal changes of the SSAT, whereas the ICV mainly influenced the interannual changes in the SSAT over East Asia. The interannual changes of the SSAT over East Asia that were influenced by the ICV are mainly manifested as the combined effects of the large-scale ocean–atmosphere circulations, which expressed 79% explanatory power on the SSAT changes.


KEYWORDS: Regional effects; Downscaling; Regional models; Climate variability

1. Introduction

It has been shown that the summer (June, July, and August) surface air temperature (SSAT) in most regions of Asia has experienced rapid warming in the past (Li et al. 2010; Hu et al. 2019), which has resulted in more and more hot summers in recent decades (Sun et al. 2014; Wang et al. 2014). Continuous warming during the summer has been observed over East Asia, but the trends in the SSAT have also varied from region to region. Based on observations, the SSATs in East Asia have shown significant increasing trends over arid and semiarid regions of northern China from 1951 to 1999; however, cooling trends have been observed in central China (Hu 2003; Gong et al. 2004; Qian and Qin 2006). Moreover, previous studies have suggested that the SSAT changes over East Asia have involved significant regional and multiple time scale characteristics.

Some studies have disclosed that there was a clear link between the internal climate variability (ICV) and the temperature at regional scales (Sánchez-Benítez et al. 2018; Kornhuber et al. 2019;

Ren et al. 2020). Feng and Wu (2020) showed that the ICV explained, at least in part, the changes in temperature over the midlatitudes of Asia. The changes in large-scale ocean–atmosphere circulations (LOACs) are regarded as the primary manifestation of ICV. Many previous studies discussed the correlation between LOACs and temperature. Wallace and Gutzler (1981) proposed that the relationships between LOACs and regional temperature anomalies over middle and high latitudes of Northern Hemisphere are considerable. The interannual and interdecadal variability of the western North Pacific subtropical high could affect the SSAT over East Asia monsoon region (Sui et al. 2007; Chen and Lu 2014a). The nonuniform warming in summer over Eurasia displayed a good correlation with the Atlantic multidecadal oscillation and the decadal changes in the Silk Road pattern (Hong et al. 2017). The interannual variation in SSAT over Northeast Asia tended to be related to the Eurasian teleconnection pattern and the East Asia–Pacific teleconnection pattern (Chen et al. 2016), and it was also significantly modulated by the East Asia

 Denotes content that is immediately available upon publication as open access.

Corresponding author: Deming Zhao, zhaodm@tea.ac.cn

Publisher's Note: This article was revised on 7 July 2022 to correct the affiliation of coauthor Shen, which was incorrect when originally published, and to add funding information in the Acknowledgments section that was originally missing.

DOI: 10.1175/JCLI-D-21-0577.1

© 2022 American Meteorological Society. For information regarding reuse of this content and general copyright information, consult the AMS Copyright Policy (www.ametsoc.org/PUBSReuseLicenses).

summer monsoon (Ding and Chan 2005). The Arctic Oscillation can be associated with the extreme summer temperature and the heat wave frequency in most regions of Northern Hemisphere midlatitudes (Tang et al. 2014; Lee and Lee 2016). The variety of the above-mentioned teleconnection patterns is indicative of the complexity of the remote circulations associated with variability in SSAT over Asia. The interactions and modulations among the different LOACs are complex (Wang et al. 2004; Deser et al. 2012a), so it is difficult to isolate and quantify the contributions of the different LOACs to temperature changes at regional scale.

In addition to the effects of ICV, the changes in external forcing (EF) also exert an important effect on SSAT changes over East Asia. Increasing concentrations of greenhouse gas (GHG) emissions have resulted in a considerable warming over East Asia in the twentieth century (Christensen et al. 2013). Nevertheless, if EFs such as total solar irradiance, ozone, and the direct effects of aerosols are considered, a cooling trend can occur over East Asia (He et al. 2013). The solar and volcanic forcings impact on the temperature over Eurasian continent have also been identified (Woollings et al. 2010; Ineson et al. 2011). Recent studies have proposed the potential causes of EF-induced cooling trends in the surface air temperature. Li et al. (2016) emphasized that the aerosol radiative effects can change the thermodynamic stability and convective potential of the lower atmosphere, which can induce the decreasing in temperature and strengthening in atmospheric stability. Moreover, different EF fields can alter monsoon circulations, which can also affect the surface air temperature (Li et al. 2007, 2016).

Hasselmann (1976) pointed out that the EF factors (e.g., GHG emissions) can leave a specific fingerprint in the climate system. By isolating this fingerprint, the effects of human activity on the climate change can be detected. This is the theoretical basis for the present studies on the detection and attribution of the climate change. Based on this statistical assumption for diagnosis, several studies have been carried out to perform the influence of ICV and EF on the climate change (Hegerl and North 1997; Hegerl et al. 2000, 2003; Sun et al. 2016; Qian and Zhang 2019). In previous studies, the optimal fingerprint is one of the commonly used methods to isolate the effects of ICV from the forced response signals (Hasselmann 1997; Stott 2003). Given that the response of climate change to EF leaves a fingerprint, the optimal fingerprint can be used to quantify the effect of a single forcing factor on climate change at given levels of uncertainty based on linear regression analysis. Large ensemble (LE) simulation is also developed to estimate the effects of EF (Deser et al. 2012a, 2014), since the internal variability of models can be eliminated based on the ensemble mean of members in LEs (Li et al. 2019). Furthermore, individual members of the LEs only differ in their initial conditions (Bittner et al. 2016), and the anomalous trend in the individual members from LEs can be attributed to the roles of ICV (Deser et al. 2012b; Hu et al. 2019). Nevertheless, in the model world, the effects of EF based on LEs can only be considered effective when the ensemble member is large enough to guarantee the statistical significance level (Monerie et al. 2017; Hu et al. 2019; Li et al. 2021). Additionally, due to the deficiencies and discrepancies among models, the ICV is different among models or

between the real world and the model world (Dai 2006; Dai and Bloecker 2019).

The effects of the ICV on temperature based on optimal fingerprints are generated with global climate models (GCMs), which are used mainly for detecting the signals of ICV and EF in temperature and analyzing the uncertainties of the results. Therefore, such results could not represent the real ICV or EF effects on temperature, which only have meaning in a statistical sense (Luo et al. 2020). The results obtained based on the LEs depend significantly on the performance of the GCMs in simulating the temperature (Zha et al. 2021a). Nevertheless, most GCMs are ineffective in simulating regional and local climate features due to their coarse resolution. Consequently, GCMs results are difficult to be directly applied at regional scale, especially over the regions with complex topography and inhomogeneous land distributions (e.g., East Asia). Previous studies have shown that the state-of-the-art coupled models have limitations in being able to reproduce climate change for East Asia (Kang et al. 2002; He et al. 2013). To overcome these limitations, high-resolution regional climate model (RCM) simulations have been used extensively for the regions with complex terrain, such as East Asia (Li et al. 2020; Wu et al. 2020; Zhao et al. 2020, 2021). Thus, the RCM could be more suitable for regions where local effects are the important processes that controlling changes in the regional climate (Gutowski et al. 2020).

The SSAT changes at regional scales are influenced by the ICV and EF, but to what extent the SSAT changes can be attributed to the ICV and EF remain key questions. Also, whether the decadal and interannual changes in the SSAT are influenced by different forcing responses. These scientific issues are yet to be resolved. In this study, a new approach is proposed based on the combined use of reanalysis data, multiple GCM outputs, and RCM simulated results, with which the effects of ICV and EF to changes in the SSAT are isolated and estimated. Compared to optimal fingerprint and LEs simulation with GCMs, this method can be more suitable to be used at regional and local scales, especially for regions with complex and heterogeneous terrain (e.g., East Asia).

2. Datasets and methods

a. Datasets

1) OBSERVATIONS

To validate the performance of the RCM in simulating the SSAT changes over East Asia, the monthly mean temperature data spanning the period from 1958 to 2001 were extracted from the gridded Climate Research Unit (CRU) time series (TS) data version 4.01 (CRU TS4.01) with a spatial resolution of 0.5° latitude/longitude (Harris et al. 2014). The CRU TS4.01 dataset is produced by the CRU at the University of East Anglia, which provides monthly variations in climate observations during the period from 1901 to 2016 on high-resolution grids. The CRU TS4.01 dataset is a monthly gridded field-based dataset with the monthly observational data calculated from the daily or subdaily data of national meteorological services and other external agencies, based on

which angular-distance weighting interpolation is adopted to produce the dataset (Harris et al. 2014). A detailed description of the CRU dataset is available in Harris et al. (2014). This dataset has been widely used for assessing climate variability and validating climate models at regional scales (Giorgi et al. 2004; Jacob et al. 2007; Xu et al. 2009; Chen and Frauenfeld 2014).

2) DRIVING FIELD DATASETS

The European Centre for Medium-Range Weather Forecasts (ECMWF) ERA-40 global reanalysis product, which has a 1.1° horizontal resolution and 24 vertical pressure levels, was selected as the driving data of the RCMs (Uppala et al. 2005). ERA-40 was selected as the driving data based on its good performance in simulating climate change over East Asia (Frauenfeld et al. 2005; Ma et al. 2008; You et al. 2013; Guo et al. 2016). It has been extensively used as the driving data of RCMs, such as the Weather Research and Forecasting (WRF) Model (Lorenz and Jacob 2010; Heikkilä et al. 2011; Huang et al. 2016). Consequently, the performance of the ERA-40 was judged to be satisfactory. Actually, the ECMWF Twentieth Century Reanalysis (ERA-20C), the National Oceanic and Atmospheric Administration Twentieth Century Reanalysis (NOAA-20CR), the Japanese 55-year atmospheric reanalysis (JRA-55), and the National Centers for Environmental Prediction–National Center for Atmospheric Research reanalysis (NCEP–NCAR) were also considered during our experimental design. However, each dataset has its own deficiencies in East Asia, including issues such as coarse spatial resolution, sharp fluctuations in the time sequence, large bias in the climatology and trends, and incorrect interannual and monthly variability (Luo et al. 2019; Shen et al. 2021a). Additionally, there is no water vapor data above 300 hPa in NCEP–NCAR and JRA-55. The ERA-Interim reanalysis product had just been released for data after 1979, and the latest ERA5 reanalysis product had not been released completely when the numerical simulation was designed and carried out. Therefore, the ERA-40 dataset was selected for this study ultimately.

The multimodel ensemble mean (MME) of Coupled Model Intercomparison Project phase 5 (CMIP5) historical outputs is also used as the lateral boundary condition of the RCM, due to the fact that CMIP6 had not been released when all experiments were designed. The CMIP5 historical runs with the monthly mean values were used this study, including air temperature, relative humidity, surface pressure, sea level pressure, zonal and meridional components of wind, and so forth. Each model had three ensemble members. Therefore, there were 51 ensemble members across all 17 models. The details for the selected 17 CMIP5 GCMs are shown in Table 1.

3) DETECTION AND ATTRIBUTION MODEL INTERCOMPARISON PROJECT

To reveal the potential causes of irregular changes in the SSAT over East Asia induced by EF, the Detection and Attribution Model Intercomparison Project (DAMIP) from

CMIP6 was used. Only 11 models of detection and attribution simulation in the DAMIP were available at the time of performing this analysis (Table 2). In this study, the impacts of two main EFs on SSAT changes over East Asia are discussed based on DAMIP: 1) aerosol forcing (anthropogenic-aerosol-only historical simulations), called the “hist-aer” experiment in DAMIP, and 2) GHG forcing (well-mixed GHG-only historical simulations), called the “hist-GHG” experiment in DAMIP. Details for the DAMIP experiments are introduced in Gillett et al. (2016).

4) CLIMATE INDICES

To investigate the possible effects of the LOACs on the SSAT changes over East Asia, 16 time series for the climate indices were selected; these included the 1) Atlantic meridional mode (AMM; Chiang and Vimont 2004); 2) Atlantic Oscillation (AO; Higgins et al. 2002); 3) East Asian summer monsoon (EASM; Li and Zeng 2002); 4) North Atlantic Oscillation (NAO; Barnston and Livezey 1987); 5) Niño-3; 6) Niño-3.4; 7) Niño-4 (Trenberth and Stepaniak 2001); 8) Pacific decadal oscillation (PDO; Mantua et al. 1997); 9) South China Sea summer monsoon (SCSSM; Li and Zeng 2003); 10) Southern Hemisphere annular mode (SHAM; Nan and Li 2003); 11) 10.7-cm solar flux (Solar; Moen and Brekke 1993); 12) tropical northern Atlantic pattern (TNA; Enfield et al. 1999); 13) Western Hemisphere warm pool (WHWP; Wang and Enfield 2001); 14) western Pacific index (WPI; Barnston and Livezey 1987); 15) western Pacific subtropical high area (WPSHA; Huang et al. 2018); and 16) western Pacific subtropical high intensity (WPSHI; Huang et al. 2018). These climate indices, which have been widely used by the research community, are informative in terms of the various fluctuations that the LOACs undergo. The physical processes of LOACs reflected by these climate indices have important effects on climate change over East Asia (Zeng et al. 2019). Consequently, these climate indices are adopted to perform this analysis. A guide to the downloading of these climate indices is available in Shen et al. (2021b).

b. Methods

1) MODEL DESCRIPTION AND EXPERIMENTAL DESIGN

The RCM used in this study is WRF version 3.8.1 with the Advanced Research version of WRF core, released on 12 August 2016. The simulation domain covers most of East Asia (0°–55°N, 57.5°–142.5°E), with a spatial resolution of 0.5° × 0.5°. The WRF simulations were integrated over 44 years from January 1958 to August 2002. Preliminary experiments were carried out to optimize the parameterization schemes (Luo et al. 2020). The main schemes used in this study are presented in Table 3. The EF in model should be varied with time for long-term climate simulation; however, most forcing variables in current available WRF versions are fixed in time at the climate mean state without interannual variabilities. Additionally, none of the radiative physical schemes has considered the effect of volcanic aerosols, which have significant impact on long-term climate evolution (Dai 2010; Diallo et al. 2017; Cooper et al. 2018; Hegerl et al. 2019).

TABLE 1. Model names, model institutions, spatial resolutions, countries, and ensemble numbers across the selected 17 Coupled Model Intercomparison Project phase 5 (CMIP5) global climate models analyzed in this study.

No.	Model name	Institution	Spatial resolution	Country	Ensembles
1	BCC Climate System Model, version 1.1 (BCC-CSM1.1)	Beijing Climate Center (BCC), China Meteorological Administration	128×64	China	3
2	Second Generation Canadian Earth System Model (CanESM2)	Canadian Centre for Climate Modeling and Analysis (CCCMA)	128×64	Canada	3
3	Community Climate System Model, version 4 (CCSM4)	National Center for Atmospheric Research (NCAR)	288×192	United States	3
4	CNRM Coupled Global Climate Model, version 5 (CNRM-CM5)	Centre National de Recherches Meteorologiques (CNRM)/Centre Europeen de Recherche et Formation Avancee en Calcul Scientifique	256×128	France	3
5	CSIRO Mark, version 3.6.0 (CSIRO-Mk3.6.0)	Commonwealth Scientific and Industrial Research Organization (CSIRO) in collaboration with Queensland Climate Change Centre of Excellence	192×96	Australia	3
6	Flexible Global Ocean–Atmosphere–Land System Model grid point, version 2 (FGOALS-g2)	State Key Laboratory of Numerical Modeling for Atmospheric Sciences and Geophysical Fluid Dynamics, Institute of Atmospheric Physical, Chinese Academy of Sciences and CESS, Tsinghua University	128×60	China	3
7	GFDL Climate Model, version 3 (GFDL CM3)	National Oceanic and Atmospheric Administration (NOAA) Geophysical Fluid Dynamics Laboratory (GFDL)	144×90	United States	3
8	GISS Model E2, coupled with the Hybrid Coordinate Ocean Model (GISS-E2-H)	National Aeronautics and Space Administration (NASA) Goddard Institute for Space Studies (GISS)	144×90	United States	3
9	GISS Model E2, coupled with the Russell Ocean model (GISS-E2-R)	NASA Goddard Institute for Space Studies	144×90	United States	3
10	Hadley Centre Coupled Model, version 3 (HadCM3)	Met Office Hadley Centre	96×73	United Kingdom	3
11	IPSL Coupled Model, version 5, coupled with Nucleus for European Modeling of the Ocean (NEMO), low resolution (IPSL-CM5A-LR)	Institute Pierre-Simon Laplace (IPSL)	96×96	France	3
12	Model for Interdisciplinary Research on Climate, Earth System Model (MIROC-ESM)	Japan Agency for Marine–Earth Science and Technology, Atmosphere and Ocean Research Institute (The University of Tokyo), and National Institute for Environment Studies	128×64	Japan	3
13	Model for Interdisciplinary Research on Climate, version 5 (MIROC5)	Center for Climate System Research (The University of Tokyo)	256×128	Japan	3
14	MPI Earth System Model, low resolution (MPI-ESM-LR)	Max Planck Institute for Meteorology (MPI)	192×96	Germany	3
15	MPI Earth System Model, intermediate resolution (MPI-ESM-MR)	MPI Earth System Model, medium resolution	192×96	Germany	3
16	MRI Coupled Atmosphere–Ocean General Circulation Model, version 3 (MRI-CGCM3)	Meteorological Research Institute (MRI)	320×160	Japan	3
17	Norwegian Earth System Model, version 1 (intermediate resolution) (NorESM1-M)	Norwegian Climate Centre	144×96	Norway	3

TABLE 2. Model names, model institutions, spatial resolutions, and countries of the 11 Detection and Attribution Model Intercomparison Project (DAMP) used in this study.

No.	Model name	Institution	Spatial resolution	Country
1	ACCESS-CM2	Commonwealth Scientific and Industrial Research Organization	145×192	Australia
2	ACCESS-ESM1-5	Commonwealth Scientific and Industrial Research Organization	145×192	Australia
3	BCC-CSM2-MR	Beijing Climate Center	64×128	China
4	CanESM5	Canadian Centre for Climate Modeling and Analysis	64×128	United States
5	CESM2	National Center for Atmospheric Research	192×288	United States
6	FGOALS-g3	Institute of Atmospheric Physics, Chinese Academy of Sciences	80×180	China
7	GFDL-ESM4	Geophysical Fluid Dynamics Laboratory	180×360	United States
8	IPSL-CM6A-LR	Institute for Pierre Simon Laplace	143×144	France
9	MIROC6	Japan Agency for Marine-Earth Science and Technology, Atmosphere and Ocean Research Institute, National Institute for Environmental Studies, PIKEN Center for Computational Science	128×256	Japan
10	MRI-ESM2-0	Meteorological Research Institute	160×320	Japan
11	NorESM2-LM	Center for International Climate and Environmental Research, Norwegian Meteorological Institute, Nansen Environmental and Remote Sensing Center, Norwegian Institute for Air Research, University of Bergen, University of Oslo	96×144	Norway

Therefore, the WRF Model is modified to include both spatially and temporally varying EF. For instance, the Thompson microphysics scheme and the RRTMG radiation transfer scheme are revised by including the 3D time varying aerosol concentrations. The spatiotemporal distributions of volcanic aerosols, ozone, and long-term variations of the solar constant are introduced in the radiative physics scheme. The Noah land surface model is modified to consider land use and cover change. The spectral nudging is applied to the air temperature, wind vector, and relative humidity above the boundary layer. The coefficient of spectral nudging is $3 \times 10^{-5} \text{ s}^{-1}$.

The method used to isolate the EF and the ICV signals based on the WRF dynamical downscaling has been

expressed systematically in the previous study (Luo et al. 2020). In this paper, the main steps of the method are given to ensure completeness in the method description. First, we use the reanalysis data (RE) as the driving field to carry out a numerical experiment (EX1). The RE can be decomposed into climate mean state ($\overline{\text{RE}}$) and the anomaly field (RE'). The driving field of EX1 is denoted as Eq. (1):

$$D_{\text{ALL}} = \text{RE} = \overline{\text{RE}} + \text{RE}'. \quad (1)$$

The reanalysis product has an assimilated observation, so the effects of both EF and ICV are included in EX1. Similarly, the MME of CMIP5 can also be decomposed into the sum of climatology ($\overline{\text{MME}}$) and anomaly (MME'). The

TABLE 3. The main parameterization schemes for WRF downscaling simulation used in the study.

Physics options	Names	Descriptions	References
Microphysics (mp_physics)	Thompson aerosol-aware microphysics scheme	This scheme considers water- and ice-friendly aerosol. A climatology dataset could be used to specify initial and boundary conditions for the aerosol variables.	Thompson and Eidhammer (2014)
Longwave radiation (rw_lw_physics)	RRTMG scheme	It includes the MCICA method of random cloud overlap. For major trace gases, $\text{CO}_2 = 379 \times 10^{-6}$, $\text{N}_2\text{O} = 319 \times 10^{-9}$, $\text{CH}_4 = 1774 \times 10^{-9}$.	Iacono et al. (2008)
Shortwave radiation (ra_sw_physics)	RRTMG shortwave	A new shortwave scheme with the MCICA method of random cloud overlap.	Iacono et al. (2008)
Planetary boundary layer (bl_pbl_physics)	YSU scheme	Non-local K scheme with explicit entrainment layer and parabolic K profile in unstable mixed layer.	Hong (2010)
(sf_surface_physics)	Noah-MP land surface model	Noah-MP contains a separate vegetation canopy defined by a canopy top and bottom with leaf physical and radiometric properties used in a two-stream canopy radiation transfer scheme that includes shading effects, which also contains a multilayer snowpack with liquid water storage and melt/refreeze capability and a snow-interception model describing loading/unloading, melt/refreeze, and sublimation of the canopy-intercepted snow.	Niu et al. (2011)
Cumulus parameterization (cu_physics)	New simplified Arakawa-Schubert	New mass-flux scheme with deep and shallow components and momentum transport.	Han and Pan (2011)

CMIP5 models have different phases for the ICV. If the sample size is sufficiently large, the ICV signals can be considered to be cancelled when the MME is calculated (Jiang et al. 2020; Tokarska et al. 2020; Ukkola et al. 2020). Therefore, we can use the MME of CMIP5 historical experiment outputs as the lateral boundary fields of the RCM. Nevertheless, the climatology simulated by GCM usually has large bias relative to observation, which would be propagated into the RCM if MME is directly used to drive RCM (Xu and Yang 2015). Therefore, the mean climate state of MME in CMIP5 ($\overline{\text{MME}}$) is replaced with the mean climate state of $\overline{\text{RE}}$ for the second experiment (EX2). The driving field of EX2 is denoted as Eq. (2):

$$D_{\text{EF}} = \overline{\text{RE}} + \text{MME}'. \quad (2)$$

In EX2, it is assumed that the CMIP5 ensemble is sufficiently large that ICV signals are cancelled when the MME is calculated, leaving just the effects of EF.

In the third experiment (EX3), the difference between the ERA-40 and anomaly value of MME is considered as the driving data of RCM, which is denoted as Eq. (3):

$$D_{\text{ICV}} = \text{RE} - \text{MME}'. \quad (3)$$

Noting that the EF and the ICV effects are included in RE, and MME' only includes the EF effect. Hence, EX3 just includes the ICV effect. A similar approach has been adopted to extract the ICV by removing the EF from the observations (Hegerl et al. 1996; Kaufmann et al. 2011; Song et al. 2014; Dai et al. 2015). A detailed outline of the technical details of the experimental design is given in Luo et al. (2020).

The output averaging frequency of the experiment with ERA-40 driving data is every 6 h. To match this experiment, the MME of CMIP5 monthly data is interpolated to 6-h intervals, which is added to the climatological mean 6-h reanalysis data to get the driving data, due to the difficulty of obtaining 6-h data for each CMIP5 model. This approach, which could neglect some signals of diurnal cycles and submonthly variability in the climate system, has been used for the long-term climate simulation in the former study (Xu and Yang 2015). In this study, we mainly focused on the interannual and the decadal changes of SSAT based on the annual mean values of SSAT. Therefore, the neglected diurnal and submonthly signals will not affect our focus. Nevertheless, it can be a better choice if the 6-h data for each CMIP5 model can be obtained.

To estimate the performance of the WRF in simulating the SSAT over East Asia, the correlation coefficient, the root-mean square error (RMSE), and the skill score between the observation and the simulation were calculated. The correlation coefficient and the RMSE have been used in many climate studies (Wu et al. 2016; Zha et al. 2019, 2020; Shen et al. 2021b), and details are not presented here. The skill score is calculated using Eq. (4):

$$\text{skill score} = \frac{(1 + R)^2}{\left(\text{SDR} + \frac{1}{\text{SDR}}\right)^2}, \quad (4)$$

where R is the spatial correlation between the observation and the simulation, and SDR is the ratio of the spatial standard deviations of the observation and the simulation. Both the spatial distribution and the magnitude are considered in the skill score. The better the relationship is, the closer the value is to 1 (Song and Zhou 2014; Peng et al. 2020).

2) PIECEWISE LINEAR FUNCTION

To investigate the changing trends of the SSAT during different periods, a piecewise linear function (PWL) is employed to quantify the potential turning point in a given sequence, due to the fact that the turning point cannot be selected optimally based on a traditional single linear method (Shen et al. 2021b,c). A PWLF can automatically detect the point where the slope of a linear function changes and identify the optimal breakpoints, allowing multiple linear models to be fitted to each distinct section of a time sequence (Fyllas et al. 2009; Jekel and Venter 2019). A PWLF can be described using Eq. (5):

$$y(t) = \begin{cases} \eta_1 + m_1(t - b_1) & b_1 < t < b_2 \\ \eta_2 + m_2(t - b_2) & b_2 < t < b_3 \\ \vdots & \vdots \\ \eta_{n_b-1} + m_{n_b-1}(t - b_{n_b-1}) & b_{n_b-1} < t < b_{n_b} \end{cases}, \quad (5)$$

where b_1 is the location of the first turning point, b_2 is the location of the second turning point, etc., to the last turning point b_{n_b} . The necessity of introducing turning point is tested statistically with a t test under the null hypothesis that m_{n_b-1} is not different from zero. We assume that the time sequence has one and only one turning point in this study. When the turning point is unknown, optimization is used to find the best set of turning point that minimize the overall sum-of-the-squares of the residual (SSR). The SSR is represented as a function dependent on the turning point. A summary of the optimization problem is as follows Eq. (6):

$$\begin{cases} \text{minimize SSR}(\mathbf{b}), \quad \mathbf{b} = [b_2, \dots, b_{n_b-1}]^T \\ \text{subject to } x_1 \leq b_k \leq x_n, \quad k = 1, 2, \dots, b_n. \end{cases} \quad (6)$$

In the PWLF, differential evolution is used for the global optimization (Storn and Price 1997). Statistical significance for the regression includes the goodness of fit, and the P values for the trends before and after turning point. Details for the PWLF can be seen in Jekel and Venter (2019).

3) FORWARD STEPWISE REGRESSION ALGORITHM

The forward stepwise regression algorithm (FSRA) is employed to pick out the dominant climate indices that have the largest explanatory power for the changes in the SSAT. Both X_i (climate indices) and Y (SSAT) are selected to establish the regression model [Eq. (7)]:

$$\begin{cases} Y = \alpha_i X_i + \beta, i = 1, 2, \dots, p \ (p = 17) \\ F^{(1)} = \max\{F_1^{(1)}, F_2^{(1)}, \dots, F_p^{(1)}\} \\ I = \{X_i | 1 < i < p\}, \end{cases} \quad (7)$$

where α_i and β are the regression coefficients and residual, respectively; $F_i^{(1)}$ is the value of the F test for α_i , and $F^{(1)}$ denotes the maximum value of $F_i^{(1)}$. Given that the threshold of the significance level $\alpha = 0.01$, if $F^{(1)} \geq F_{\alpha}^{(1)}$, X_i is introduced into the model. The term I_1 denotes the set of introduced X_i . When X_i is selected, the bivariate regression is estimated between Y and the subsets $\{X_i, X_1\}, \dots, \{X_i, X_{i-1}\}, \{X_i, X_{i+1}\}, \dots, \{X_i, X_p\}$ ($p - 1$ subsets). Similarly, the statistical value of the F test is $F_{X_k}^{(2)}$ ($X_k \neq I_1$), and the maximum $F_{X_k}^{(2)}$ is selected. If $F_{X_k}^{(2)} \geq F_{\alpha}^{(2)}$, X_k is input into the model. Using the FSRA, a reconstructed SSAT is obtained based on the selected climate indices and their regression coefficients, as expressed in Eq. (8):

$$\text{SSAT}_R = \sum_{i=1}^6 a_i X_i + b_0, \quad (8)$$

where a_i and b_0 are the regression coefficients and residual, respectively. To evaluate the importance of the selected climate indices and test the uncertainty of the reconstructed SSAT, we randomly select a 30% subset of the grids and perform the FSRA 300 times.

A Gaussian low-pass filter with a 9-yr window is used to extract the decadal signals in the time sequence (Zhu et al. 2012), and the interannual sequence of the data is obtained based on the raw sequence minus the decadal sequence (Wu et al. 2018a; Shen et al. 2021a). The linear trend is calculated using the least squares method, and the significance of trend and correlation coefficient is determined using the two-tailed Student's t test (Zha et al. 2016; Zhao et al. 2021).

3. Results

a. Evaluating the performance of the WRF in simulating the SSAT changes in East Asia

The climatology and the linear trend of the SSAT in the WRF downscaling simulation (EX1) and the reanalysis output are compared with the observation for a 44-yr period (Fig. 1). The results show that the spatial patterns of the SSATs in the WRF downscaling simulation and the reanalysis output were consistent with those in the observation (Figs. 1a–c), with the spatial correlations being 0.97 ($p < 0.01$) and 0.92 ($p < 0.01$), respectively. Compared to the reanalysis output, the regional and local characteristics of the SSAT could be better captured by the WRF downscaling simulation. Based on the inspection of observation, the SSAT experienced a significant warming over most regions of East Asia, especially for the regions to north of 40°N, where the warming trend reached 0.3°C decade^{−1} ($p < 0.01$). The observed SSAT showed a decrease over the southern parts of the Tibetan Plateau and southeastern China, although the decreasing trend failed Student's t test at the 0.01 significance level (Fig. 1d). The cooling trend over southeastern China is also reported by He

et al. (2013). The simulated spatial pattern of SSAT trend with WRF was similar to those of the observation over East Asia, such as the cooling over the southern parts of Tibetan Plateau and southeastern China, and the warming over the Indian peninsula and the Indo-China peninsula. Nevertheless, the warming in the WRF downscaling simulation was weaker than those in the observation, and the simulated SSAT showed a decreasing trend in scattered areas over the regions north of 40°N (Fig. 1e), which could be attributed to the systematic model bias (Luo et al. 2020). The reanalysis output can reproduce the main characteristics of the observed SSAT trends over East Asia, but failed to reproduce the warming over northwestern China (Fig. 1f).

Temporal evolutions of the regional mean SSAT in the observation, the RCM downscaling, and the reanalysis output are exhibited in Fig. 2. The observed SSAT showed a decreasing trend from 1958 to 1972 and an increasing trend after 1972, at rates of $-0.14^\circ\text{C decade}^{-1}$ ($p < 0.01$) and $0.24^\circ\text{C decade}^{-1}$ ($p < 0.01$), respectively (Fig. 2a). Compared to the observation, the WRF downscaling simulation also underwent a decreasing trend from 1958 to 1972 and an increasing trend after 1972, at rates of $-0.31^\circ\text{C decade}^{-1}$ ($p < 0.01$) and $0.16^\circ\text{C decade}^{-1}$ ($p < 0.01$), respectively (Fig. 2b). The correlation coefficient of temporal sequences between the observation and the WRF simulation was 0.87 ($p < 0.01$). Reanalysis output studied here failed to capture the decadal changes of the observed SSAT over East Asia. Based on the PWLF, the turning point of the SSAT in the reanalysis output was located in 1993, which was not consistent with the observation (Fig. 2c). Additionally, the SSAT in the reanalysis output exhibited a pronounced peak from 1958 to 1966, which was not apparent in the observation. Compared to Fig. 1, the decreasing trends of SSAT over some regions of East Asia could be caused mainly by the cooling before 1972. We also compared the spatial pattern of the trends during two periods (figures not shown). Before (after) 1972, both observed and simulated SSAT mainly showed decreasing (increasing) trends over most regions of East Asia. Therefore, the downward trend in earlier period followed by upward trend in later period can be found in most regions of East Asia. This characteristic was also reported in an independent study (Chen and Lu 2014b).

Based on the aforementioned results, it is concluded that the WRF downscaling simulation better captured the spatio-temporal characteristics of the observed SSAT over East Asia than the reanalysis output analyzed here. To quantitatively estimate the relationship between the observation and the RCM downscaling simulation, the correlation coefficient, the RMSE, and the skill score between the observation and the WRF simulation were computed (Fig. 3). The observation and WRF simulation showed a significant positive correlation, which passed Student's t test at the 0.10 significance level for the study region (Fig. 3a). The regional mean correlation coefficient reached 0.62 ($p < 0.10$). The regional mean RMSE was 1.38°C with the large values locating mainly in western China, and small values of the RMSEs locating mainly in eastern China (Fig. 3b). The RMSEs were larger over western China and Tibetan Plateau than those over eastern China, which could be a reflection of the complex and/or

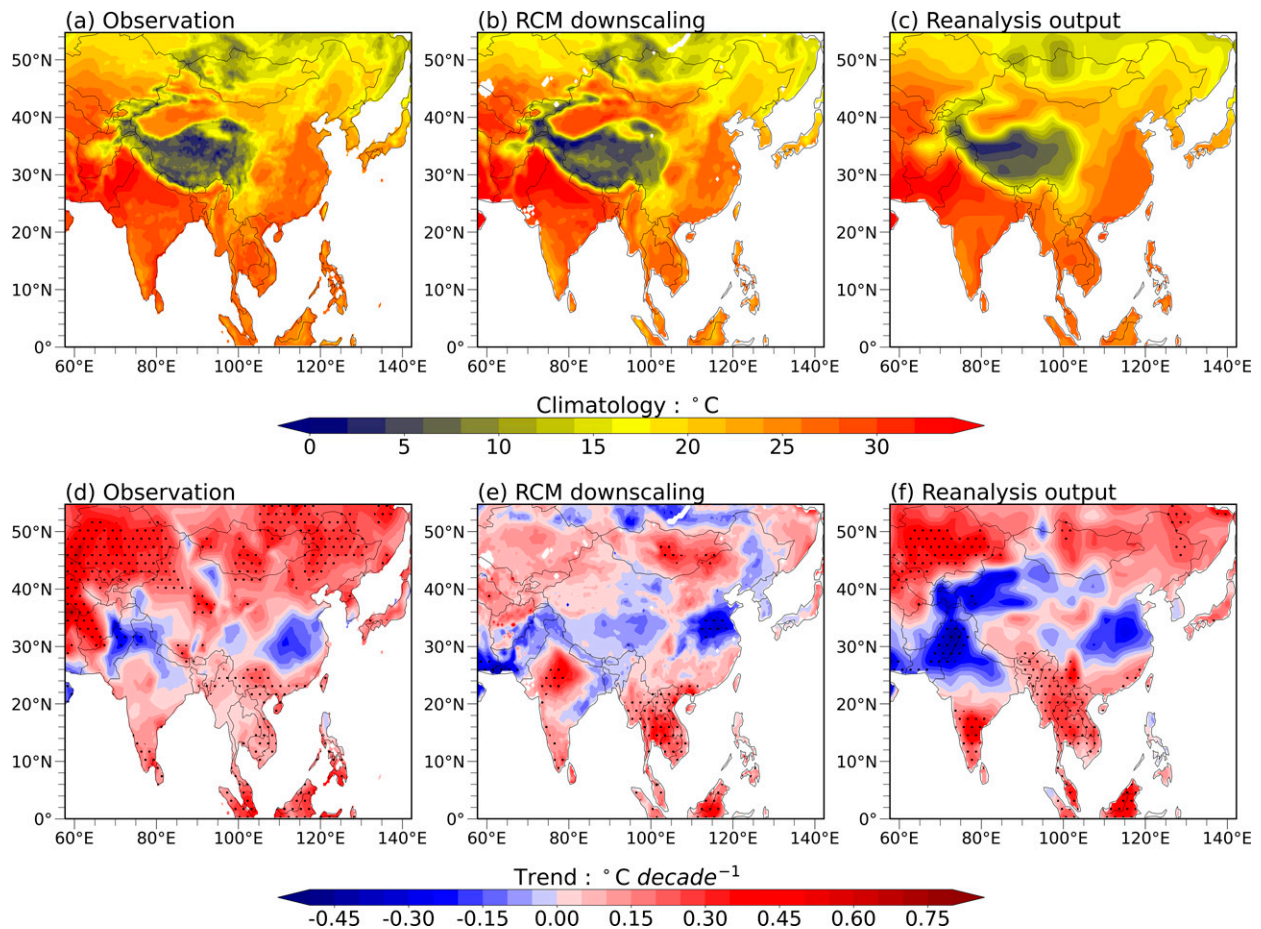


FIG. 1. Spatial patterns of (top) the averaged summer surface air temperature (SSAT) ($^{\circ}\text{C}$) and (bottom) the trends of the SSAT $^{\circ}\text{C decade}^{-1}$ over East Asia during the period from 1958 to 2001, for (a),(d) observation, (b),(e) RCM downscaling simulation, and (c),(f) ERA-40 reanalysis output. Dots in (d)–(f) indicate that trends pass Student's t test at the 0.01 significance level.

heterogeneous terrain; moreover, these local effects cannot be well reproduced in the model (Li et al. 2020). The regional mean skill score was 0.62. The large values of the skill score located mainly in regions north of 40°N (>0.7), and the small

values located mainly in the Indian peninsula (<0.5) (Fig. 3c). Compared to the ERA-40 reanalysis output, the WRF downscaling simulation can better capture the atmospheric meso-scale features and the land surface heterogeneity at finer

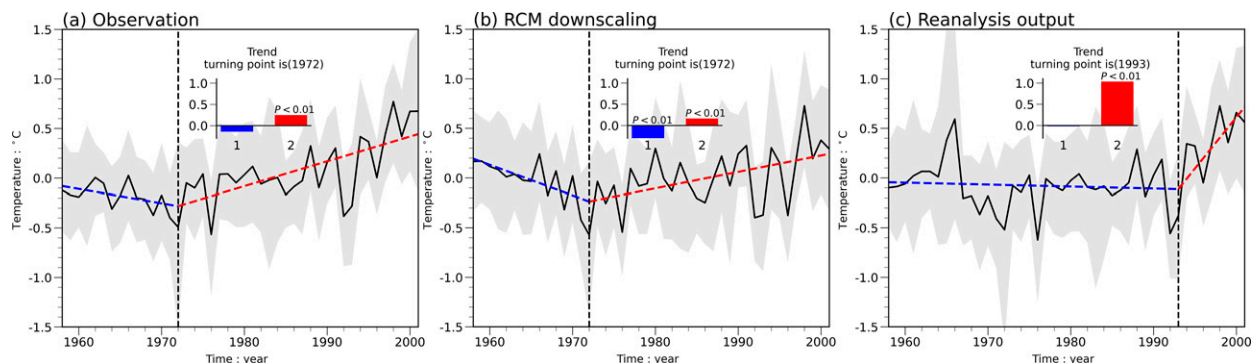


FIG. 2. Temporal evolutions of the averaged summer surface air temperature (SSAT) anomaly during the period from 1958 to 2001 with (a) observation, (b) RCM downscaling simulation, and (c) reanalysis output. Blue and red lines denote the piecewise linear function (PWL) fitting curves. The shaded regions represent the ranges of the 25th and 75th percentiles of SSAT in all grids. In the inset, the blue and red bars denote the trends during different periods; $p < 0.01$ denotes the PWLF fitting passes Student's t test at the 0.01 significance level. Calculations are based on the area-averaging of entire study region as shown in Fig. 1.

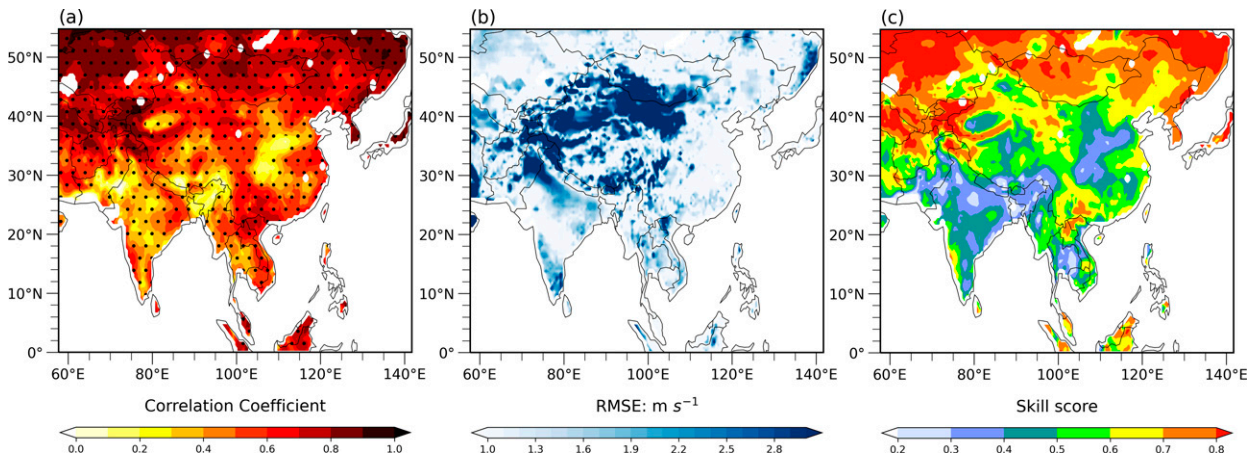


FIG. 3. Spatial patterns of (a) correlation coefficient, (b) root-mean square error ($^{\circ}\text{C}$), and (c) skill score between the observation SSAT and the simulation SSAT. Dots in (a) denote the correlation coefficients pass Student's t test at the 0.10 significance level.

scale. Furthermore, due to the model improvement and the optimization of parameterization schemes in WRF, the dynamics and thermodynamics components at finer scale could also be better captured by the WRF downscaling simulation. As a consequence, the WRF downscaling simulation had multiple improvements over the reanalysis data studied here, and therefore better reproduced the main characteristics of the SSAT changes over East Asia.

b. Effects of EF and ICV to the SSAT changes over East Asia

The potential influences of the EF and ICV on the spatio-temporal changes in SSAT over East Asia will be discussed in this section. Based on Eqs. (2) and (3) in section 2b, the EF and the ICV affect the SSAT changes over East Asia are differentiated. The spatial patterns of the climatology and the trends for the SSAT with the EF and the ICV responses are shown in Fig. 4. The climatological SSAT under EF response was consistent with those under the ICV (Figs. 4a,b). Spatial distributions of the simulated SSAT from EF and ICV were similar to those as shown in Fig. 1a. However, the SSAT with EF underwent a significant enhancement over most regions of East Asia, for which the trends passed Student's t test at the 0.01 significance level (Fig. 4c). Noting that the SSAT with EF also showed a reduction over some regions of the Indian peninsula, the Indo-China peninsula, and the middle and lower reaches of the Yellow River valley in China. The potential causes could be attributed mainly to aerosol emissions (Li et al. 2016). The cooling trend in the SSAT over the middle and lower reaches of the Yellow River valley in China was also reported in He et al. (2013). In section 4b, the potential causes of the cooling trend over the aforementioned regions will be discussed. The ICV mainly induced a decrease in the SSAT over East Asia except for northern India and Indo-China peninsula, although the trends failed to pass Student's t test (Fig. 4d). Compared to Fig. 1d, the warming trend over most regions of East Asia could be attributed mainly to EF response, and the ICV could cause cooling in East Asia.

Compared to Fig. 1e, we can note that the combination of the EF and the ICV (Figs. 4c,d) were similar to the result shown in Fig. 1e. It was also found that the local maximums appearing in northern India, the Indo-China Peninsula, and eastern Mongolia in Fig. 1 were realized in ICV experiment (Fig. 4d). Furthermore, the strong negative trend along 30° – 35°N presented in Fig. 1e is also found in Fig. 4d. These results may imply an important role of ICV in determining the SSAT trend in those regions.

The effects of EF and ICV on the temporal evolutions of the SSAT were also revealed (Fig. 5). Compared to Fig. 2, the changes of the SSAT with EF were similar to the observation and all forcings. The SSAT with EF response exhibited a decrease before 1965 and an increase thereafter, at rates of $-0.52^{\circ}\text{C decade}^{-1}$ ($p < 0.01$) and $0.16^{\circ}\text{C decade}^{-1}$ ($p < 0.01$), respectively (Fig. 5a). Nevertheless, the temporal evolutions of the SSAT with the ICV were not consistent with the observation. The SSAT with the ICV showed a decreasing trend over the whole study period ($-0.09^{\circ}\text{C decade}^{-1}$; $p < 0.01$), which did not exhibit the change from decrease to increase (Fig. 5b). The correlation coefficients between all forcings and EF, and between all forcings and ICV, were 0.65 ($p < 0.01$) and -0.54 ($p < 0.01$), respectively. Based on six CMIP5 GCMs and a statistical diagnosis analysis method, Qian and Zhang (2019) also reported that the temporal evolutions of SSAT with ICV cannot matched well with the observed SSAT over China. They found that all EF contributed 100% of the observed change in the amplitude in SSAT over China, whereas the natural variability showed negative contributions for SSAT changes. Hence, compared to a previous study, our results can also be confirmed.

The changes of the SSAT included the decadal and the interannual changes. To detect how the SSAT was influenced by the EF and the ICV at different time scales, the temporal evolutions of the SSAT with different forcing responses were compared at the decadal and the interannual scales. The results show that the decadal changes in the SSAT with EF were consistent with all forcings, with a correlation coefficient

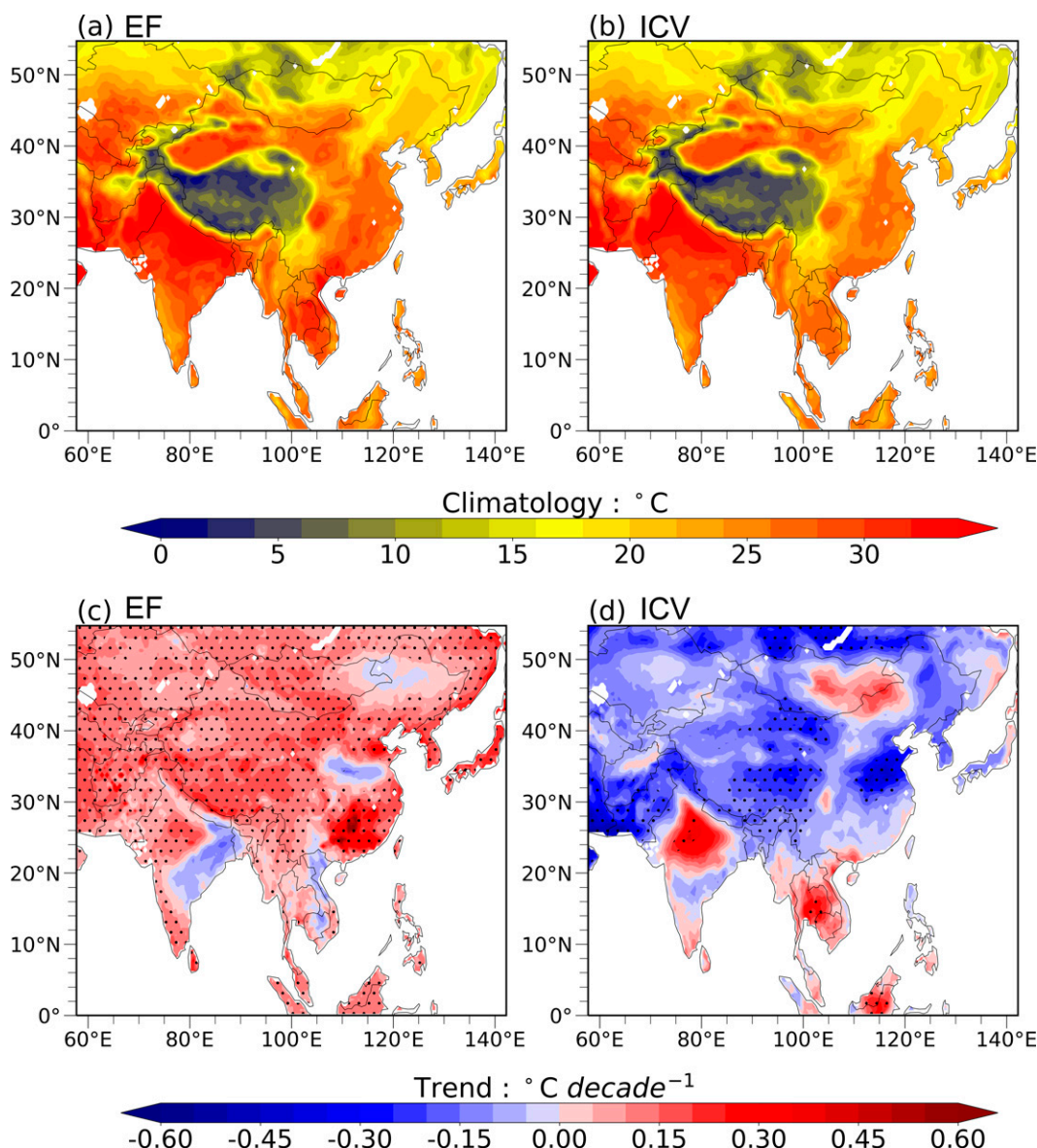


FIG. 4. Spatial patterns of (top) the averaged summer surface air temperature (SSAT) (°C) and (bottom) the trends of SSAT (°C decade⁻¹) with (a),(c) external forcing (EF) and (b),(d) internal climate variability (ICV) over East Asia during the period from 1958 to 2001. In (c) and (d), dots denote the trends pass Student's *t* test at the 0.01 significance level.

of 0.72 ($p < 0.01$). The decadal changes of the SSAT with the ICV were significantly different for all forcings, whereas the interannual changes of the SSAT with the ICV were consistent with all forcings. At the interannual scale, the probability of SSAT with all forcings and SSAT with ICV having extreme values at the same time point can reach 90%, whereas the probability of SSAT with all forcings and SSAT with EF having extreme values at the same time point was less than 20%. Furthermore, at the interannual scale, the correlation coefficient between SSAT with the all forcings and SSAT with the EF (ICV) was 0.50 (0.80). These results imply that the decadal and the interannual changes of the SSATs over East Asia

could be attributed mainly to the EF and the ICV responses, respectively.

4. Discussion

a. Potential manifestation of the ICV impacts on the SSAT changes over East Asia

The above-mentioned results indicate that the ICV has a considerable influence on the interannual changes of the SSAT over East Asia. Generally, the ICV is manifested mainly by the changes of the LOACs, such as the EASM (Ding and Chan 2005), the NAO (Sun et al. 2008), ENSO

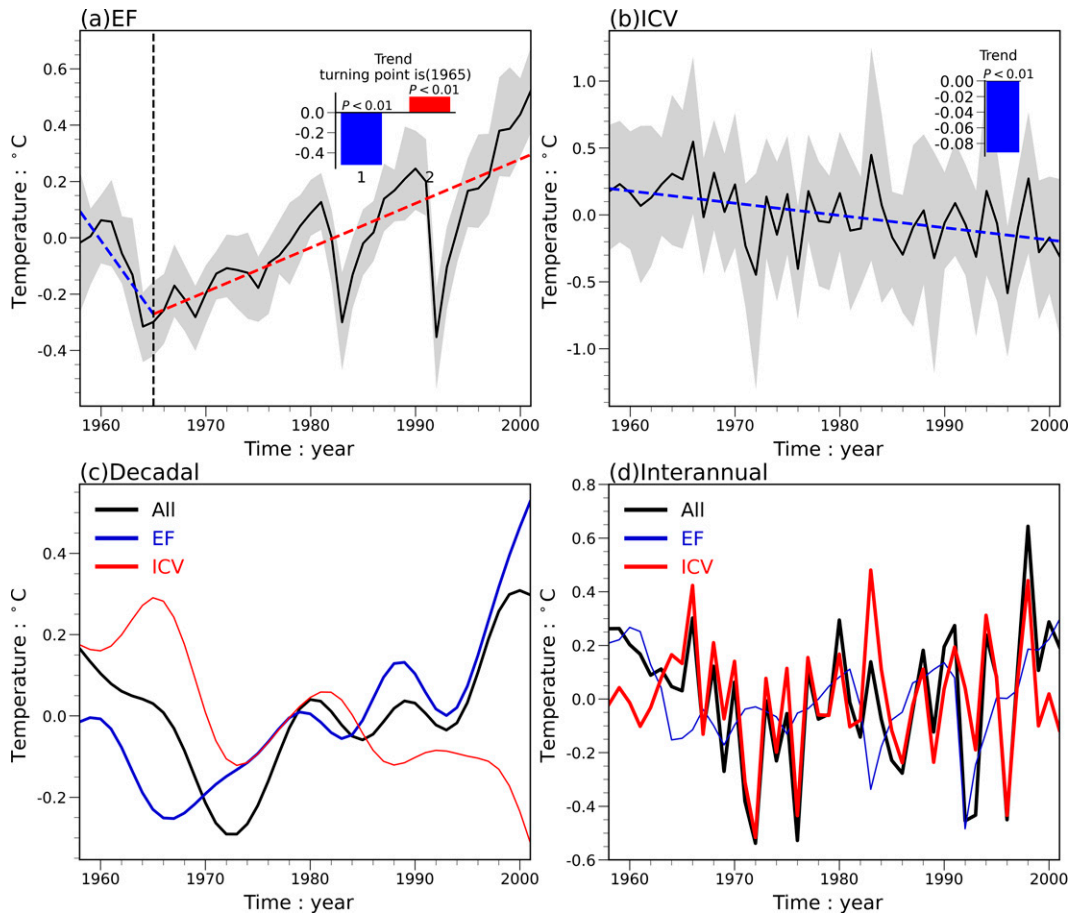


FIG. 5. Temporal evolutions of the averaged summer surface air temperature (SSAT) anomalies during the period from 1958 to 2001 with (a) external forcing (EF) and (b) internal climate variability (ICV), and the temporal evolutions of SSAT during the period from 1958 to 2001 at (c) the decadal scale and (d) the interannual scale. In (a) and (b), the shaded regions represent the ranges of the 25th and 75th percentiles of SSAT in all grids. Blue and red lines denote the piecewise linear function (PWLf) fitting curves. In the insets in (a) and (b), the blue and red bars denote the trends of SSAT during different periods, and $p < 0.01$ denotes that the PWLF fitting passes Student's t test at the 0.01 significance level. In (c) and (d), the black, blue, and red lines denote all forcings, EF, and ICV, respectively.

(Lim and Kim 2013), the AO (He et al. 2017), the WPSH (Liu et al. 2019), the SCSSM (You et al. 2021), and so forth, which have been suggested to exert influences on the SSAT over East Asia. In this section, the LOACs that could influence the changes of the SSAT over East Asia were examined based on the FSRA. To avoid overfitting, six primary climate indices that explain the changes in the SSAT were validated based on their statistical significance (Shen et al. 2021b; Zha et al. 2021b). This preprocessing method has been used in the previous study (Zeng et al. 2019). Actually, it was noted that the improvement in fit became marginal when the number of climate indices retrained in the stepwise regression became relatively large (e.g., the explanatory power changed by only 5% in going from 6 to 12 indices). Based on FSRA, the selected six climate indices were the Niño-3.4, NAO, PDO, SCSSM, Niño-4, and WPI. The total explanatory power for the selected indices was 79%, which passed Student's t test at the 0.01 significance level. To evaluate the uncertainty of the

selection, 300 random samples (30% of the grids were chosen at random for each experiment) were performed to determine if the selected six indices could be selected for most cases. The results revealed that the selected six indices can be selected in all 300 experiments, but for WPI.

According to Eqs. (7) and (8), a reconstructed SSAT (called $SSAT_R$ hereafter) can be obtained, and then the $SSAT_R$ was compared with the SSAT that included only by the ICV response (called $SSAT_{ICV}$ hereafter). The results show that the $SSAT_R$ matched well the $SSAT_{ICV}$ for the whole study period (Fig. 6a), which could suggest a predictive relationship between SSAT changes and LOACs. The correlation coefficient between the $SSAT_R$ and the $SSAT_{ICV}$ reached 0.79 ($p < 0.01$). The probability density function (PDF) of the $SSAT_R$ was similar to those of the $SSAT_{ICV}$. Both the PDF of $SSAT_R$ and the PDF of $SSAT_{ICV}$ were centered on zero, although the $SSAT_R$ was narrower than $SSAT_{ICV}$ (Fig. 6b). These results imply that the $SSAT_R$ was

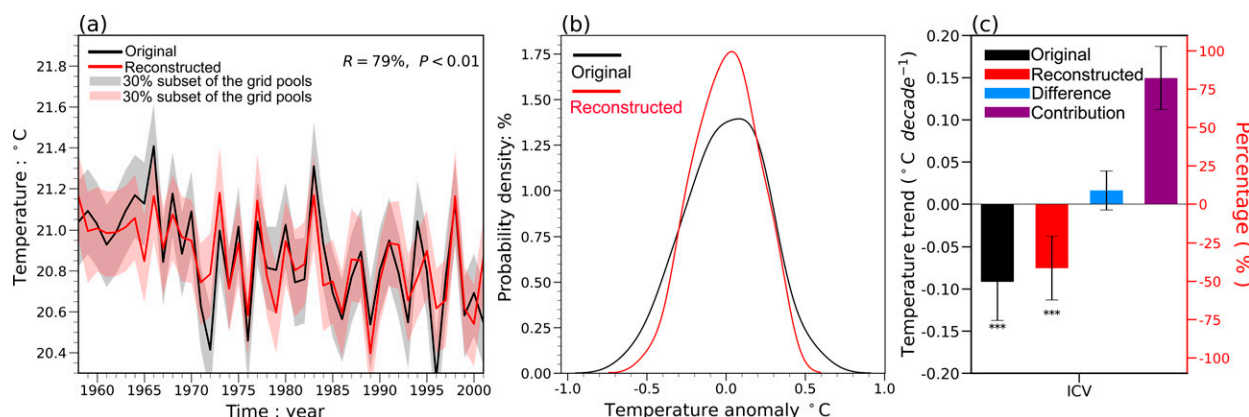


FIG. 6. (a) Temporal evolutions of SSAT_{ICV} (black lines) and SSAT_R (red lines), (b) probability density function curves of the SSAT_{ICV} and SSAT_R anomalies, and (c) linear trends of the SSAT_{ICV} and SSAT_R (°C decade⁻¹), and their difference, as well as the relative contributions of the primary LOACs to the long-term changes in the SSAT_{ICV}. In (a), uncertainties are represented by the interquartile range of the results based on a randomly selected 30% subset of the grid pools in East Asia (repeated 300 times). Inset numbers are the correlation coefficients and their significance between the SSAT_{ICV} and the SSAT_R. In (c), three asterisks (***) denote Student's *t* test at the 0.001 significance level. The black bars denote the uncertainty ranges of results. Difference denotes the difference in trends between the SSAT_{ICV} and the SSAT_R.

capable of reproducing the SSAT changes with the ICV. Given that the SSAT_R can reproduce the temporal evolutions of the SSAT_{ICV}, the contributions of the LOACs to the trend of the SSAT_{ICV} can be evaluated. Both the SSAT_{ICV} and the SSAT_R exhibited decreasing trends, but the reduction of the SSAT_R ($-0.075^{\circ}\text{C decade}^{-1}$; $p < 0.001$) was slower than those of the SSAT_{ICV} ($-0.091^{\circ}\text{C decade}^{-1}$; $p < 0.001$), with the difference being $0.016^{\circ}\text{C decade}^{-1}$. The contribution of the selected LOACs to the downward trend of the SSAT_{ICV} was 82.4% (Fig. 6c). These results imply that the decrease of the SSAT induced by the ICV over East Asia could be attributed mainly to the combined effects of variations in the selected six LOACs. Actually, the correlations between the SSAT_{ICV} and all 16 climate indices were also compared, showing that no single index had a large explanatory power on the SSAT changes. However, a large explanatory power was generated when the indices were taken together. Consequently, the interannual changes in the SSAT_{ICV} over East Asia cannot be simply linked to just one LOAC, but should be determined by the combined effects of variations in the selected six LOACs.

Several previous studies have proposed that the ICV has a considerable effect on the regional temperature changes (Deser et al. 2012a; Sánchez-Benítez et al. 2018; Kornhuber et al. 2019); however, the EF effects are not excluded. Therefore, the quantitative effects of a single ICV realization on the SSAT changes over East Asia could show uncertainty (Ding and Chan 2005; Chen and Lu 2014a; Lee and Lee 2016; Hong et al. 2017). In this study, the results suggested that the ICV could cause cooling in East Asia. It must also be stated that the predictors are not independent; that is, the interactions and modulations among different LOACs are considerable (Gong and Ho 2003; Wang et al. 2004). For instance, the SCSSM onset can be influenced by El Niño events (Hu et al. 2020), the phase changes in the PDO have a propensity to

coincide with changes in the relative frequency of ENSO events (Verdon and Franks 2006), ENSO can affect the NAO (Mokhov and Smirnov 2006), the PDO shows interannual modulation on the low-latitude western North Pacific (Wu 2013), and so forth. A previous study has shown that the non-independence of LOAC indices could influence the standard deviations of the reconstructed sequences (Shen et al. 2021b). Additionally, the LOACs could also include the EF signals, which was not excluded in the present study. These uncertainties ultimately lead to conclusion that the SSAT_R cannot explain entirely the variabilities and the magnitude of the trend in the SSAT_{ICV}. Whether the nonlinear relationship between the SSAT_{ICV} and the LOACs can better express the influences of LOACs on the SSAT_{ICV} changes than linear one is unclear. How to best clarify the physical mechanisms whereby the combined effects of the various LOACs affect the SSAT_{ICV} over East Asia are topics of great interest that need to be addressed in future research.

In addition to the above-mentioned LOACs, some other teleconnection patterns, such as the east Atlantic/west Russian (WA/WR) teleconnection and Scandinavian pattern explain the large-scale Rossby-wave propagation originating from the North Atlantic and Scandinavian Peninsula, may influence the temperature over East Asia. Nevertheless, some studies have pointed out that the WA/WR teleconnection pattern mainly influences surface temperature over North America, North Africa, Middle East, and Europe (Lim 2015). The Scandinavian pattern is found to exhibit apparent seasonality in its spatial structure and dynamical properties, and mainly influences the temperature over the Eurasian continent during winter and spring. During summer, the Scandinavian pattern is weak and can be neglected (Bueh and Nakamura 2007). Therefore, the Scandinavian pattern could generate weak effects on summer temperature changes over East Asia. Additionally, some LOACs, such as AMM, TNA,

and SHAM, mainly representing the climate variations over the Atlantic region or Southern Hemisphere, have negligible impact on the SSAT variability over East Asia.

b. Potential causes of uneven changes in the SSAT induced by EF

Based on interpretation of Fig. 4c, the warming in East Asia was considered to be induced by EF. However, EF also caused a decrease of the SSAT over some regions of the Indian peninsula and the Indo-China peninsula. This raises a question of whether these are valid signals or if this is a result of bias in the WRF downscaling simulation, which needs to be clarified. The WRF downscaling simulation can isolate the effects of the EF on the SSAT changes, but it cannot determine the primary EF signals inducing the SSAT changes. To address this question, 11 DAMIP models from the CMIP6 are used. Before the detection and attribution analysis was carried out, the performance of the DAMIP in simulating the SSAT changes over East Asia was analyzed. The results show that the MME of DAMIP were capable of reproducing the spatiotemporal characteristics of the SSAT over East Asia. The spatial distribution of the SSAT in the MME of DAMIP was consistent with those of the observation (Fig. 7a), with a spatial correlation coefficient of 0.92 ($p < 0.01$). The temporal evolutions of the SSAT in the MME of DAMIP were also consistent with those of the observation (Fig. 7b), with a correlation coefficient of 0.79 ($p < 0.001$). To quantify the relationship between the observation and the MME of DAMIP, the correlation coefficient, the RMSE, and the skill score were calculated (Fig. 8). The observation and the MME of DAMIP showed positive correlation, passing Student's t test at the 0.10 significance level for most regions. The regional mean RMSE and skill score were 2.01°C and 0.35, respectively. Consequently, the DAMIP data were capable of capturing the spatiotemporal characteristics of the SSAT over East Asia. Compared to Fig. 3, the RMSE between the observation and the DAMIP was larger than those between the observation and the WRF downscaling simulation, whereas the correlation coefficient and the skill score between the observation and the DAMIP were smaller than those between the observation and the WRF downscaling simulation. Most of current GCMs are run with a coarse resolution, which cannot accurately represent temperature changes at finer scale, since the atmospheric mesoscale features and the land surface heterogeneity cannot be properly resolved by the GCMs (Fu et al. 2005; Xu and Yang 2015). Additionally, the WRF has been fed the correct ICV, whereas the DAMIP simulations have arbitrary ICV. Accordingly, the performance of WRF downscaling in simulating the SSAT over East Asia is better than the DAMIP.

In this study, two main kinds of EF, aerosol forcing and GHG forcing, have been discussed. The spatial patterns of the trends in the SSAT with different forcing responses are shown in Fig. 9. During the study period, accompanied by aerosol forcing, the SSAT mainly decreased, particularly strongly in the Indian peninsula, Indo-China peninsula, and

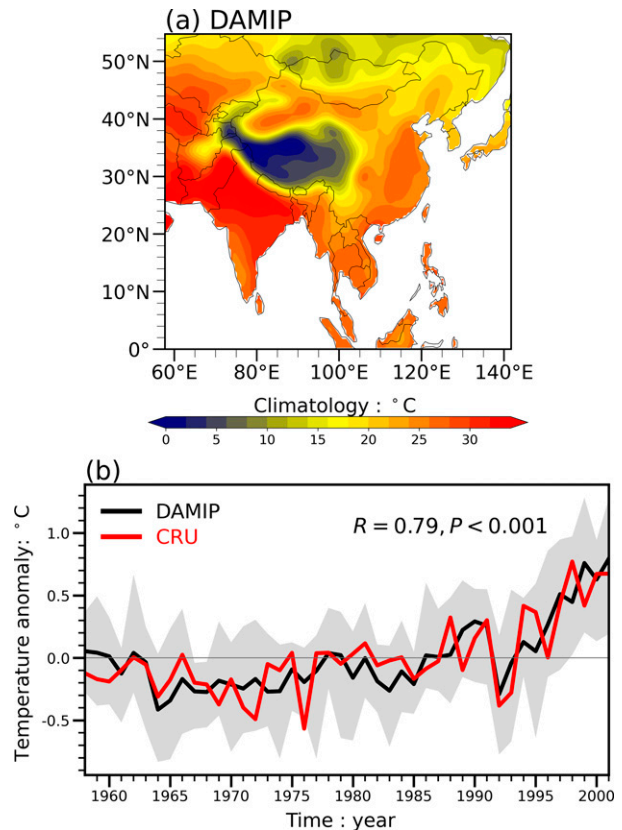


FIG. 7. (a) Spatial pattern of the averaged summer surface air temperature (SSAT) in the multimodel ensemble mean (MME) of 11 Detection and Attribution Model Intercomparison Project (DAMIP) models (°C), and (b) temporal evolutions of the SSAT anomaly from 1958 to 2001 in the MME of DAMIP (black line) and the observation (red line). The shading denotes the uncertainty spread determined by all DAMIP models; R denotes the correlation coefficient between the MME of DAMIP and the observation for the SSAT, and $p < 0.001$ denotes that the correlation coefficient passes Student's t test at the 0.001 significance level.

eastern China. The cooling even exceeded $-0.3^{\circ}\text{C decade}^{-1}$ ($p < 0.10$) in the Indian peninsula (Fig. 9a). For the GHG forcing, the SSAT mainly increased, which was particularly strong in regions north of 40°N and the Tibetan Plateau (Fig. 9b). If both the aerosol and the GHG forcings are considered (Fig. 9c), a cooling was found over the Indian peninsula and the Shandong peninsula. Compared to Fig. 4c, the cooling in the Indian peninsula based on WRF downscaling simulation should be induced mainly by aerosol forcing, and which should not be the systematic bias in the WRF downscaling simulation. Therefore, the uneven changes of the trend in the SSAT induced by EF may be attributed mainly to the heterogeneous distribution of aerosols. In this study, we mainly detected the possible causes of cooling induced by EF in some regions of the Indian peninsula and the Indo-China peninsula. The physical mechanisms of how GHGs and aerosols affect the temperature changes have been discussed

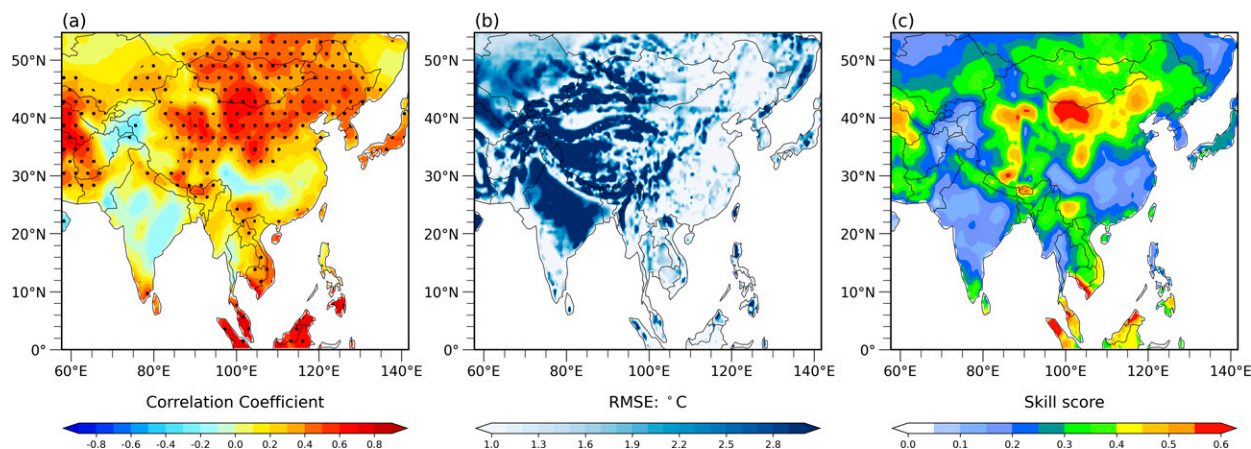


FIG. 8. Spatial patterns of (a) correlation coefficient, (b) root-mean square error, and (c) skill score between observation and multimodel ensemble mean of DAMIP. Dots in (a) denote that the correlation coefficients pass Student's t test at the 0.10 significance level.

extensively in the former studies (Jain 1993; Ramanathan and Feng 2009; He et al. 2013; Li et al. 2016; Huang et al. 2017), which are not the focus of this study and will not be discussed here. It is worth noting that except for the GHGs and aerosols, the EF also includes land use and cover change (LUCC) and urbanization (Zha et al. 2017; Wu et al. 2018b). Some studies have expounded on the influences of LUCC and urbanization on temperature changes (Kalnay and Cai 2003; Pitman et al. 2012; Zhao et al. 2018). Therefore, the uneven changes in the trends of the SSAT induced by EF may also be partially attributable to the LUCC and urbanization.

5. Conclusions

In this study, based on a WRF downscaling simulation, the influences of EF and ICV on the SSAT changes over East Asia are estimated. The potential manifestation of how the ICV influences the SSAT changes and the potential causes of the uneven changes in the SSAT induced by EF are discussed. The main results are summarized as follows:

- 1) The RCM downscaling simulation had multiple improvements over the driving data. It can better capture the spatiotemporal characteristics of the observed SSAT over East Asia than the reanalysis output studied here. Compared to the reanalysis output used here, the RCM downscaling simulation can better reproduce the regional and local characteristics of the climatological SSAT over East Asia. However, the warming trend in the RCM downscaling simulation was weaker than those in the observation. The observed SSAT experienced a decadal transition in the study period, exhibiting a significant decrease from 1958 to 1972 ($-0.14^{\circ}\text{C decade}^{-1}$) and a significant strengthening thereafter ($0.24^{\circ}\text{C decade}^{-1}$). These observed characteristics can be reproduced by the RCM downscaling simulation, but cannot be captured by the reanalysis output studied here. The correlation coefficient and the skill score between the observation and the RCM downscaling simulation were higher than those between the observation and the reanalysis output studied here, and the RMSE between the observation and the RCM

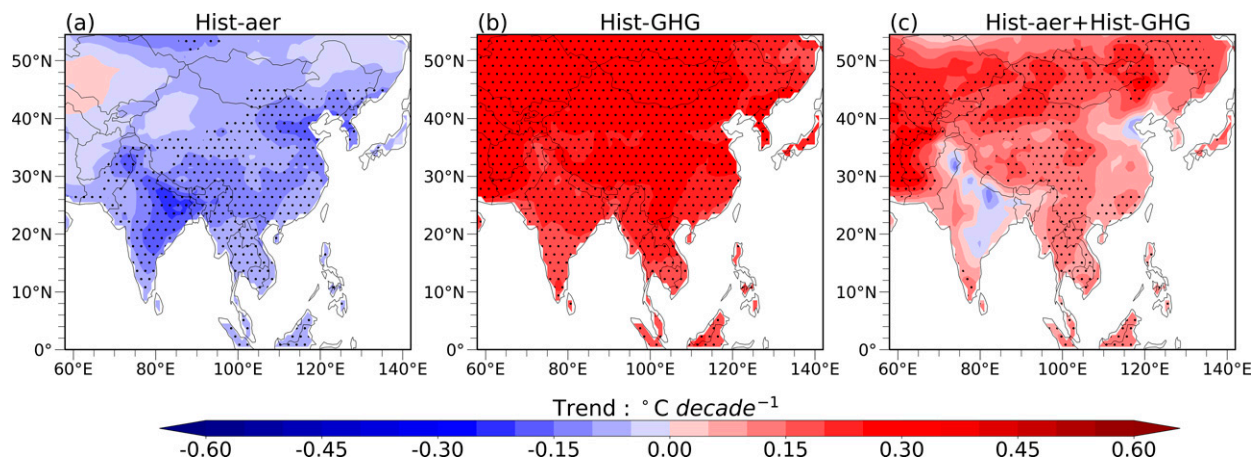


FIG. 9. Spatial patterns of the trend in the summer surface air temperature (SSAT) of the multimodel ensemble mean in DAMIP ($^{\circ}\text{C decade}^{-1}$) over East Asia during the period from 1958 to 2001 with (a) aerosol forcing, (b) GHG forcing, and (c) aerosol and GHG forcings combined. The dots indicate that the trends pass Student's t test at the 0.10 significance level.

downscaling simulation was lower than that between the observation and the reanalysis output studied here.

- 2) The SSAT climatology in East Asia with EF response was similar to those with the ICV response, which indicate that the EF and the ICV did not alter the spatial pattern of the SSAT climatology. However, the SSAT with EF showed significant warming over most regions of East Asia, but for some regions of the Indian peninsula and the Indo-China peninsula. The SSAT with the ICV showed cooling over East Asia, except for northern India and the Indo-China peninsula. Therefore, the warming over most regions of East Asia could be attributed mainly to EF, whereas the ICV could cause cooling in East Asia. The decadal changes of the SSAT under all forcings were consistent with those under the EF, and the interannual changes of the SSAT under all forcings were consistent with those under the ICV. Hence, the decadal and the interannual changes of the SSAT over East Asia could be dominated by the EF and the ICV, respectively.
- 3) The ICV, which impacted the SSAT over East Asia, was caused by processes represented by the climate indices, and the crucial climate indices were the Niño-3.4, NAO, PDO, SCSSM, Niño-4, and WPI. The total explanatory power of these selected LOACs to the SSAT changes that induced by ICV reached 79%. Therefore, the interannual changes of the SSAT_{ICV} over East Asia cannot be simply linked with just one LOAC, but should be determined by the combined effects of the variations in the various LOACs. Based on the FSRA, the SSAT_R matched the SSAT_{ICV} well for the whole study period and was capable of capturing the SSAT_{ICV} changes. The quantitative results show that the contribution of the LOACs to the downward trend of the SSAT_{ICV} reached 82.4%. Furthermore, based on the DAMIP, the SSAT mainly displayed decreasing and increasing trends over East Asia accompanied by the aerosol and GHG forcings, respectively. If both the aerosol and GHG forcings are considered, a cooling for the study period can be found over the Indian peninsula and the Shandong Peninsula. Therefore, the uneven changes of the trend in the SSAT induced by EF may be dominated by the heterogeneous distribution of aerosols.

The effects of ICV and EF on the SSAT changes over East Asia are isolated and quantified in this study. However, there are limitations and drawbacks that are necessary to be mentioned. In this paper, we just qualitatively estimate the effects of primary LOACs on the SSAT changes over East Asia; thus, this just be a result of diagnostic analysis. It does not mean that the SSAT changes are entirely determined by the selected six climate indices. Furthermore, we also noted that the ICV has influences on SSAT changes over East Asia with marked regional differences, such as the SSAT over the Indian peninsula and the Indo-China peninsula shows opposed trends compared to other regions, which may be attributed to the effects of the Indian Ocean dipole mode (IODM) on the temperature changes over southern part of East Asia. Some previous studies have pointed out that IODM can

modulate ENSO (Izumo et al. 2010) and the East Asian summer monsoon (Yuan et al. 2008), which is associated with the climate and monsoon variability over India (Ashok et al. 2004; Kripalani and Kumar 2004) and East Asia (including the Indo-China peninsula) (Guan and Yamagata 2003; Kripalani et al. 2005, 2010). Nevertheless, how to demonstrate the physical mechanisms of ICV influencing the SSAT over East Asia needs to be further investigated in the future.

Additionally, the CMIP5 and the ERA-40 datasets are used as the lateral boundary condition of the WRF downscaling simulation. Meanwhile, all of model improvements and test of parameterization schemes are carried out based on $0.5^\circ \times 0.5^\circ$ resolution. Due to the high cost of long-term climate simulation, we do not have enough computing and storage resources to carry out the numerical simulation with finer resolution at present. In the future, based on different lateral boundary condition datasets (e.g., CMIP6, ERA5, etc.) and finer spatial resolution, the uncertainties of EF and ICV governing the SSAT changes over East Asia at different time scales can be further evaluated.

Acknowledgments. We cordially thank the reviewers for their thorough comments and constructive suggestions. The work is supported by National Key Research and Development Program of China (2018YFA0606004 and 2016YFA0600403), Natural Science Foundation of China (42005023, 41875178), Nanjing Meteorological Bureau Scientific Project (NJ202103), and Swedish Formas (2019-00509 and 2017-01408) and VR (2021-02163 and 2019-03954). This work is also supported by the Program for Key Laboratory in University of Yunnan Province, the High-level Talents Program of Yunnan University, and the Chinese Jiangsu Collaborative Innovation Center for Climate Change. The authors declare no competing interests.

Data availability statement. The data that support the findings of this study are openly available at <https://esgf-node.llnl.gov/projects/cmip6/>.

REFERENCES

- Ashok, K., Z. Guan, N. H. Saji, and T. Yamagata, 2004: Individual and combined influences of ENSO and the Indian Ocean dipole on the Indian summer monsoon. *J. Climate*, **17**, 3141–3155, [https://doi.org/10.1175/1520-0442\(2004\)017<3141:IAOCIE>2.0.CO;2](https://doi.org/10.1175/1520-0442(2004)017<3141:IAOCIE>2.0.CO;2).
- Barnston, A. G., and R. E. Livezey, 1987: Classification, seasonality and persistence of low-frequency atmospheric circulation patterns. *Mon. Wea. Rev.*, **115**, 1083–1126, [https://doi.org/10.1175/1520-0493\(1987\)115<1083:CSAPOL>2.0.CO;2](https://doi.org/10.1175/1520-0493(1987)115<1083:CSAPOL>2.0.CO;2).
- Bittner, M., H. Schmidt, C. Timmreck, and F. Sienz, 2016: Using a large ensemble of simulations to assess the Northern Hemisphere stratospheric dynamical response to tropical volcanic eruptions and its uncertainty. *Geophys. Res. Lett.*, **43**, 9324–9332, <https://doi.org/10.1002/2016GL070587>.
- Bueh, C., and H. Nakamura, 2007: Scandinavian pattern and its climatic impact. *Quart. J. Roy. Meteor. Soc.*, **133**, 2117–2131, <https://doi.org/10.1002/qj.173>.
- Chen, L., and O. W. Frauenfeld, 2014: Surface air temperature changes over the twentieth and twenty-first centuries in

- China simulated by 20 CMIP5 models. *J. Climate*, **27**, 3920–3937, <https://doi.org/10.1175/JCLI-D-13-00465.1>.
- Chen, W., and R. Lu, 2014a: The interannual variation in monthly temperature over northeast China during summer. *Adv. Atmos. Sci.*, **31**, 515–524, <https://doi.org/10.1007/s00376-013-3102-3>.
- , and —, 2014b: A decadal shift of summer surface air temperature over northeast Asia around the mid-1990s. *Adv. Atmos. Sci.*, **31**, 735–742, <https://doi.org/10.1007/s00376-013-3154-4>.
- , X. Hong, R. Lu, A. Jin, S. Jin, J. C. Nam, and B. J. Kim, 2016: Variation in summer surface air temperature over northeast Asia and its associated circulation anomalies. *Adv. Atmos. Sci.*, **33** (1), 1–9, <https://doi.org/10.1007/s00376-015-5056-0>.
- Chiang, J. C. H., and D. J. Vimont, 2004: Analogous Pacific and Atlantic meridional modes of tropical atmosphere–ocean variability. *J. Climate*, **17**, 4143–4158, <https://doi.org/10.1175/JCLI4953.1>.
- Christensen, J. H., K. K. Kanikicharla, G. Marshall, and J. Turner, 2013: Climate phenomena and their relevance for future regional climate change. *Climate Change 2013: The Physical Science Basis*. Cambridge University Press, 1217–1308, <https://doi.org/10.1017/CBO9781107415324.028>.
- Cooper, C. L., G. T. Swindles, I. P. Savov, A. Schmidt, and K. L. Bacon, 2018: Evaluating the relationship between climate change and volcanism. *Earth Sci. Rev.*, **177**, 238–247, <https://doi.org/10.1016/j.earscirev.2017.11.009>.
- Dai, A. G., 2006: Precipitation characteristics in eighteen coupled climate models. *J. Climate*, **19**, 4605–4630, <https://doi.org/10.1175/JCLI3884.1>.
- , and C. E. Bloecker, 2019: Impacts of internal variability on temperature and precipitation trends in large ensemble simulations by two climate models. *Climate Dyn.*, **52**, 289–306, <https://doi.org/10.1007/s00382-018-4132-4>.
- , J. C. Fyfe, S. P. Xie, and X. G. Dai, 2015: Decadal modulation of global surface temperature by internal climate variability. *Nat. Climate Change*, **5**, 555–599, <https://doi.org/10.1038/nclimate2605>.
- Dai, J. C., 2010: Volcanoes and climate. *Climatic Change*, **1**, 824–839, <https://doi.org/10.1002/wcc.76>.
- Deser, C., R. Knutti, S. Solomon, and A. S. Phillips, 2012a: Communication of the role of natural variability in future North American climate. *Nat. Climate Change*, **2**, 773–779, <https://doi.org/10.1038/nclimate1562>.
- , A. S. Phillips, V. Bourdette, and H. Teng, 2012b: Uncertainty in climate change projections: The role of internal variability. *Climate Dyn.*, **38**, 527–546, <https://doi.org/10.1007/s00382-010-0977-x>.
- , —, M. A. Alexander, and B. V. Smoliak, 2014: Projecting North American climate over the next 50 years: Uncertainty due to internal variability. *J. Climate*, **27**, 2271–2296, <https://doi.org/10.1175/JCLI-D-13-00451.1>.
- Diallo, M., and Coauthors, 2017: Significant contributions of volcanic aerosols to decadal changes in the stratospheric circulation. *Geophys. Res. Lett.*, **44**, 10 780–10 791, <https://doi.org/10.1002/2017GL074662>.
- Ding, Y. H., and J. C. Chan, 2005: The East Asian summer monsoon: An overview. *Meteor. Atmos. Phys.*, **89**, 117–142, <https://doi.org/10.1007/s00703-005-0125-z>.
- Enfield, D. B., A. M. Mestas-Núñez, D. A. Mayer, and L. Cid-Serrano, 1999: How ubiquitous is the dipole relationship in tropical Atlantic sea surface temperature? *J. Geophys. Res.*, **104**, 7841–7848, <https://doi.org/10.1029/1998JC900109>.
- Feng, X. F., and L. G. Wu, 2020: The contribution of internal variability to Asian midlatitude warming. *J. Climate*, **34**, 2429–2439, <https://doi.org/10.1175/JCLI-D-20-0231.1>.
- Frauenfeld, O. W., T. Zhang, and M. C. Serreze, 2005: Climate change and variability using European Center for Medium-Range Weather Forecasts reanalysis (ERA-40) temperatures on the Tibetan Plateau. *J. Geophys. Res.*, **110**, D02101, <https://doi.org/10.1029/2004JD005230>.
- Fu, C. B., and Coauthors, 2005: Regional Climate Model Intercomparison Project for Asia. *Bull. Amer. Meteor. Soc.*, **86**, 257–266, <https://doi.org/10.1175/BAMS-86-2-257>.
- Fyllas, N. M., and Coauthors, 2009: Basin-wide variations in foliar properties of Amazonian forest: Phylogeny, soil and climate. *Biogeosciences*, **6**, 2677–2708, <https://doi.org/10.5194/bg-6-2677-2009>.
- Gillett, N. P., and Coauthors, 2016: The Detection and Attribution Model Intercomparison Project (DAMIP v1.0) contribution to CMIP6. *Geosci. Model Dev.*, **9**, 3685–3697, <https://doi.org/10.5194/gmd-9-3685-2016>.
- Giorgi, F., X. Bi, and J. S. Pal, 2004: Mean, interannual variability and trends in a regional climate change experiment over Europe. I. Present-day climate (1961–1990). *Climate Dyn.*, **22**, 733–756, <https://doi.org/10.1007/s00382-004-0409-x>.
- Gong, D. Y., and C. H. Ho, 2003: Arctic oscillation signals in the East Asian summer monsoon. *J. Geophys. Res.*, **108**, 4066–4071, <https://doi.org/10.1029/2002JD002193>.
- , Y. Z. Pan, and J. A. Wang, 2004: Changes in extreme daily mean temperatures in summer in eastern China during 1955–2000. *Theor. Appl. Climatol.*, **77**, 25–37, <https://doi.org/10.1007/s00704-003-0019-2>.
- Guan, Z., and T. Yamagata, 2003: The unusual summer of 1994 in East Asia: IOD teleconnections. *Geophys. Res. Lett.*, **30**, 1544–1547, <https://doi.org/10.1029/2002GL016831>.
- Guo, Y., S. Zhang, J. Yan, Z. Chen, and X. Ruan, 2016: A comparison of atmospheric temperature over China between radiosonde observations and multiple reanalysis datasets. *J. Meteor. Res.*, **30**, 242–257, <https://doi.org/10.1007/s13351-016-5169-0>.
- Gutowski, W. J., Jr., and Coauthors, 2020: The ongoing need for high-resolution regional climate models: Process understanding and stakeholder information. *Bull. Amer. Meteor. Soc.*, **101**, E664–E683, <https://doi.org/10.1175/BAMS-D-19-0113.1>.
- Han, J., and H. L. Pan, 2011: Revision of convection and vertical diffusion schemes in the NCEP Global Forecast System. *Wea. Forecasting*, **26**, 520–533, <https://doi.org/10.1175/WAF-D-10-05038.1>.
- Harris, I., P. D. Jones, T. J. Osborn, and D. H. Lister, 2014: Updated high-resolution grids of monthly climatic observations—The CRU TS3.10 dataset. *Int. J. Climatol.*, **34**, 623–642, <https://doi.org/10.1002/joc.3711>.
- Hasselmann, K., 1976: Stochastic climate models: Part I. Theory. *Tellus*, **28**, 473–485, <https://doi.org/10.3402/tellusa.v28i6.11316>.
- , 1997: Multi-pattern fingerprint method for detection and attribution of climate change. *Climate Dyn.*, **13**, 601–611, <https://doi.org/10.1007/s003820050185>.
- He, B., Q. Bao, J. Li, G. Wu, Y. Liu, X. Wang, and Z. Sun, 2013: Influences of external forcing changes on the summer cooling trend over East Asia. *Climatic Change*, **117**, 829–841, <https://doi.org/10.1007/s10584-012-0592-4>.

- He, S., Y. Gao, F. Li, H. Wang, and Y. He, 2017: Impact of Arctic Oscillation on the East Asian climate: A review. *Earth Sci. Rev.*, **164**, 48–62, <https://doi.org/10.1016/j.earscirev.2016.10.014>.
- Hegerl, G. C., and G. R. North, 1997: Comparison of statistically optimal approaches to detecting anthropogenic climate change. *J. Climate*, **10**, 1125–1133, [https://doi.org/10.1175/1520-0442\(1997\)010<1125:COSOAT>2.0.CO;2](https://doi.org/10.1175/1520-0442(1997)010<1125:COSOAT>2.0.CO;2).
- , H. von Storch, K. Hasselmann, B. D. Santer, U. Cubasch, and P. D. Jones, 1996: Detecting greenhouse-gas-induced climate change with an optimal fingerprint method. *J. Climate*, **9**, 2281–2306, [https://doi.org/10.1175/1520-0442\(1996\)009<2281:DGGICC>2.0.CO;2](https://doi.org/10.1175/1520-0442(1996)009<2281:DGGICC>2.0.CO;2).
- , P. A. Stott, M. R. Allen, J. F. B. Mitchell, S. F. B. Tett, and U. Cubasch, 2000: Optimal detection and attribution of climate change: Sensitivity of results to climate model differences. *Climate Dyn.*, **16**, 737–754, <https://doi.org/10.1007/s003820000071>.
- , T. J. Crowley, S. K. Baum, K. Y. Kim, and W. T. Hyde, 2003: Detection of volcanic, solar and greenhouse gas signals in paleo-reconstructions of Northern Hemispheric temperature. *Geophys. Res. Lett.*, **30**, 1242, <https://doi.org/10.1029/2002GL016635>.
- , and Coauthors, 2019: Causes of climate change over the historical record. *Environ. Res. Lett.*, **14**, 123006, <https://doi.org/10.1088/1748-9326/ab4557>.
- Heikkilä, U., A. Sandvik, and A. Sorteberg, 2011: Dynamical downscaling of ERA-40 in complex terrain using the WRF regional climate model. *Climate Dyn.*, **37**, 1551–1564, <https://doi.org/10.1007/s00382-010-0928-6>.
- Higgins, R. W., A. Leetmaa, and V. E. Kousky, 2002: Relationships between climate variability and winter temperature extremes in the United States. *J. Climate*, **15**, 1555–1572, [https://doi.org/10.1175/1520-0442\(2002\)015<1555:RBCVAW>2.0.CO;2](https://doi.org/10.1175/1520-0442(2002)015<1555:RBCVAW>2.0.CO;2).
- Hong, S. Y., 2010: A new stable boundary-layer mixing scheme and its impact on the simulated East Asian summer monsoon. *Quart. J. Roy. Meteor. Soc.*, **136**, 1481–1496, <https://doi.org/10.1002/qj.665>.
- Hong, X., R. Lu, and S. Li, 2017: Amplified summer warming in Europe–West Asia and northeast Asia after the mid-1990s. *Environ. Res. Lett.*, **12**, 094007, <https://doi.org/10.1088/1748-9326/aa7909>.
- Hu, K., G. Huang, and X. S. Ping, 2019: Assessing the internal variability in multi-decadal trends of summer surface air temperature over East Asia with a large ensemble of GCM simulations. *Climate Dyn.*, **52**, 6229–6242, <https://doi.org/10.1007/s00382-018-4503-x>.
- Hu, P., W. Chen, S. Chen, Y. Liu, and R. Huang, 2020: Extremely early summer monsoon onset in the South China Sea in 2019 following an El Niño event. *Mon. Wea. Rev.*, **148**, 1877–1890, <https://doi.org/10.1175/MWR-D-19-0317.1>.
- Hu, Z. Z., 2003: Long-term climate variations in China and global warming signals. *J. Geophys. Res.*, **108**, 4614, <https://doi.org/10.1029/2003JD003651>.
- Huang, D., J. Zhu, Y. Zhang, Y. Huang, and X. Kuang, 2016: Assessment of summer monsoon precipitation derived from five reanalysis datasets over East Asia. *Quart. J. Roy. Meteor. Soc.*, **142**, 108–119, <https://doi.org/10.1002/qj.2634>.
- Huang, J. P., and Coauthors, 2017: Dryland climate change: Recent progress and challenges. *Rev. Geophys.*, **55**, 719–778, <https://doi.org/10.1002/2016RG000550>.
- Huang, Y., B. Wang, X. Li, and H. Wang, 2018: Changes in the influence of the western Pacific subtropical high on Asian summer monsoon rainfall in the late 1900s. *Climate Dyn.*, **51**, 443–455, <https://doi.org/10.1007/s00382-017-3933-1>.
- Iacono, M. J., J. S. Delamere, E. J. Mlawer, M. W. Shephard, S. A. Clough, and W. D. Collins, 2008: Radiative forcing by long-lived greenhouse gases: Calculations with the AER radiative transfer models. *J. Geophys. Res.*, **113**, D13103, <https://doi.org/10.1029/2008JD009944>.
- Ineson, S., A. A. Scaife, J. R. Knight, J. C. Mannes, N. J. Dunstone, L. J. Gray, and J. D. Haigh, 2011: Solar forcing of winter climate variability in the Northern Hemisphere. *Nat. Geosci.*, **4**, 753–757, <https://doi.org/10.1038/ngeo1282>.
- Izumo, T., and Coauthors, 2010: Influence of the state of the Indian Ocean dipole on the following year's El Niño. *Nat. Geosci.*, **3**, 168–172, <https://doi.org/10.1038/ngeo760>.
- Jacob, D., and Coauthors, 2007: An inter-comparison of regional climate models for Europe: Model performance in present-day climate. *Climatic Change*, **81**, 31–52, <https://doi.org/10.1007/s10584-006-9213-4>.
- Jain, P. C., 1993: Greenhouse effect and climate changes: Scientific basis and overview. *Renew. Energy*, **3**, 403–420, [https://doi.org/10.1016/0960-1481\(93\)90108-S](https://doi.org/10.1016/0960-1481(93)90108-S).
- Jekel, C., and G. Venter, 2019: pwlf: A Python library for fitting 1D continuous piecewise linear functions. GitHub, https://github.com/cjekel/piecewise_linear_fit_py.
- Jiang, J., T. Zhou, X. Chen, and L. Zhang, 2020: Future changes in precipitation over central Asia based on CMIP6 projections. *Environ. Res. Lett.*, **15**, 054009, <https://doi.org/10.1088/1748-9326/ab7d03>.
- Kalnay, E., and M. Cai, 2003: Impact of urbanization and land-use change on climate. *Nature*, **423**, 528–531, <https://doi.org/10.1038/nature01675>.
- Kang, I.-S., and Coauthors, 2002: Intercomparison of the climatological variations of Asian summer monsoon precipitation simulated by 10 GCMs. *Climate Dyn.*, **19**, 383–395, <https://doi.org/10.1007/s00382-002-0245-9>.
- Kaufmann, R. K., H. Kauppi, M. L. Mann, and J. H. Stock, 2011: Reconciling anthropogenic climate change with observed temperature 1998–2008. *Proc. Natl. Acad. Sci. USA*, **108**, 11 790–11 793, <https://doi.org/10.1073/pnas.1102467108>.
- Kornhuber, K., S. Osprey, D. Coumou, S. Petri, V. Petoukhov, S. Rahmstor, and L. Gray, 2019: Extreme weather events in early summer 2018 connected by a recurrent hemispheric wave-7 pattern. *Environ. Res. Lett.*, **14**, 054002, <https://doi.org/10.1088/1748-9326/ab13bf>.
- Kripalani, R. H., and P. Kumar, 2004: Northeast monsoon rainfall variability over south peninsular India vis-a-vis the Indian Ocean dipole mode. *Int. J. Climatol.*, **24**, 1267–1282, <https://doi.org/10.1002/joc.1071>.
- , J. H. Oh, J. H. Kang, S. S. Sabade, and A. Kulkarni, 2005: Extreme monsoons over East Asia: Possible role of Indian Ocean zonal mode. *Theor. Appl. Climatol.*, **82**, 81–94, <https://doi.org/10.1007/s00704-004-0114-z>.
- , —, and H. S. Chaudhari, 2010: Delayed influence of the Indian Ocean dipole mode on the East Asia–west Pacific monsoon: Possible mechanism. *Int. J. Climatol.*, **30**, 197–209, <https://doi.org/10.1002/joc.1890>.
- Lee, W. S., and M. I. Lee, 2016: Interannual variability of heat waves in South Korea and their connection with large-scale atmospheric circulation patterns. *Int. J. Climatol.*, **36**, 4815–4830, <https://doi.org/10.1002/joc.4671>.
- Li, D., J. Feng, A. Dosio, J. Qi, Z. Xu, and B. Yin, 2020: Historical evaluation and future projections of 100-m wind energy

- potentials over CORDEX-East Asia. *J. Geophys. Res. Atmos.*, **125**, e2020JD032874, <https://doi.org/10.1029/2020JD032874>.
- Li, J. P., and Q. C. Zeng, 2002: A unified monsoon index. *Geophys. Res. Lett.*, **29**, 1274, <https://doi.org/10.1029/2001GL013874>.
- , and —, 2003: A new monsoon index and the geographical distribution of the global monsoons. *Adv. Atmos. Sci.*, **20**, 299–302, <https://doi.org/10.1007/s00376-003-0016-5>.
- Li, L., B. Wang, and T. Zhou, 2007: Contribution of natural and anthropogenic forcing to the summer cooling over eastern China: An AGCM study. *Geophys. Res. Lett.*, **34**, L18807, <https://doi.org/10.1029/2007GL030541>.
- Li, Q., W. Dong, W. Li, X. Gao, P. D. Jones, J. Kennedy, and D. E. Parker, 2010: Assessment of the uncertainties in temperature change in China during the last century. *Chin. Sci. Bull.*, **55**, 1974–1982, <https://doi.org/10.1007/s11434-010-3209-1>.
- Li, W., Y. Chen, and W. Chen, 2021: The emergence of anthropogenic signal in mean and extreme precipitation trend over China by using two large ensembles. *Environ. Res. Lett.*, **16**, 014052, <https://doi.org/10.1088/1748-9326/abd26d>.
- Li, Z., and Coauthors, 2016: Aerosol and monsoon climate interactions over Asia. *Rev. Geophys.*, **54**, 866–929, <https://doi.org/10.1002/2015RG000500>.
- , Y. Sun, T. Li, Y. Ding, and T. Hu, 2019: Future changes in East Asian summer monsoon circulation and precipitation under 1.5 to 5°C of warming. *Earth's Future*, **7**, 1391–1406, <https://doi.org/10.1029/2019EF001276>.
- Lim, Y. K., 2015: The East Atlantic/West Russia (EA/WR) teleconnection in the North Atlantic: Climate impact and relation to Rossby wave propagation. *Climate Dyn.*, **44**, 3211–3222, <https://doi.org/10.1007/s00382-014-2381-4>.
- , and H. D. Kim, 2013: Impact of the dominant large-scale teleconnections on winter temperature variability over East Asia. *J. Geophys. Res. Atmos.*, **118**, 7835–7848, <https://doi.org/10.1002/jgrd.50462>.
- Liu, Q., T. Zhou, H. Mao, and C. Fu, 2019: Decadal variations in the relationship between the western Pacific subtropical high and summer heat waves in East China. *J. Climate*, **32**, 1627–1640, <https://doi.org/10.1175/JCLI-D-18-0093.1>.
- Lorenz, P., and D. Jacob, 2010: Validation of temperature trends in the ensembles regional climate model runs driven by ERA40. *Climate Res.*, **44**, 167–177, <https://doi.org/10.3354/cr00973>.
- Luo, M., J. Feng, Z. Xu, and Y. Wang, 2019: Evaluating the performance of five twentieth-century reanalysis datasets in reproducing the severe drought in northern China during the 1920s–1930s. *Theor. Appl. Climatol.*, **137**, 187–199, <https://doi.org/10.1007/s00704-018-2591-5>.
- , —, —, L. Chen, J. Wang, Y. Wang, S. Lin, and L. Zhong, 2020: Decadal wintertime temperature changes in East Asia during 1958–2001 and the contributions of internal variability and external forcing. *J. Geophys. Res. Atmos.*, **125**, e2019JD031840, <https://doi.org/10.1029/2019JD031840>.
- Ma, L., T. Zhang, Q. Li, O. W. Frauenfeld, and D. Qin, 2008: Evaluation of ERA-40, NCEP-1, and NCEP-2 reanalysis air temperature with ground-based measurements in China. *J. Geophys. Res.*, **113**, D15115, <https://doi.org/10.1029/2007JD009549>.
- Mantua, N. J., S. R. Hare, Y. Zhang, J. M. Wallace, and S. C. Francis, 1997: A Pacific interdecadal climate oscillation with impacts on salmon production. *Bull. Amer. Meteor. Soc.*, **78**, 1069–1080, [https://doi.org/10.1175/1520-0477\(1997\)078<1069:APICOW>2.0.CO;2](https://doi.org/10.1175/1520-0477(1997)078<1069:APICOW>2.0.CO;2).
- Moen, J., and A. Brekke, 1993: The solar flux influence on quiet time conductances in the auroral ionosphere. *Geophys. Res. Lett.*, **20**, 971–974, <https://doi.org/10.1029/92GL02109>.
- Mokhov, I. I., and D. A. Smirnov, 2006: El Niño–Southern Oscillation drives North Atlantic Oscillation as revealed with nonlinear techniques from climatic indices. *Geophys. Res. Lett.*, **33**, L03708, <https://doi.org/10.1029/2005GL024557>.
- Monerie, P. A., E. Sanchez-Gomez, B. Pohl, J. Robson, and B. Dong, 2017: Impact of internal variability on projections of Sahel precipitation change. *Environ. Res. Lett.*, **12**, 114003, <https://doi.org/10.1088/1748-9326/aa8cda>.
- Nan, S., and J. Li, 2003: The relationship between the summer precipitation in the Yangtze River valley and the boreal spring Southern Hemisphere annular mode. *Geophys. Res. Lett.*, **30**, 2266, <https://doi.org/10.1029/2003GL018381>.
- Niu, G., and Coauthors, 2011: The community Noah land surface model with multiparameterization options (Noah-MP): 1. Model description and evaluation with local-scale measurements. *J. Geophys. Res.*, **116**, D12109, <https://doi.org/10.1029/2010JD015139>.
- Peng, D., T. Zhou, L. Zhang, W. Zhang, and X. Chen, 2020: Observationally constrained projection of the reduced intensification of extreme climate events in Central Asia from 0.5°C less global warming. *Climate Dyn.*, **54**, 543–560, <https://doi.org/10.1007/s00382-019-05014-6>.
- Pitman, A. J., and Coauthors, 2012: Effects of land cover change on temperature and rainfall extremes in multi-model ensemble simulations. *Earth Syst. Dyn.*, **3**, 213–231, <https://doi.org/10.5194/esd-3-213-2012>.
- Qian, C., and X. Zhang, 2019: Changes in temperature seasonality in China: Human influences and internal variability. *J. Climate*, **32**, 6237–6249, <https://doi.org/10.1175/JCLI-D-19-0081.1>.
- Qian, W., and A. Qin, 2006: Spatial-temporal characteristics of temperature variation in China. *Meteor. Atmos. Phys.*, **93**, 1–16, <https://doi.org/10.1007/s00703-005-0163-6>.
- Ramanathan, V., and Y. Feng, 2009: Air pollution, greenhouse gases and climate change: Global and regional perspective. *Atmos. Environ.*, **43**, 37–50, <https://doi.org/10.1016/j.atmosenv.2008.09.063>.
- Ren, L., T. Zhou, and W. Zhang, 2020: Attribution of the record-breaking heat event over Northeast Asia in summer 2018: The role circulation. *Environ. Res. Lett.*, **15**, 054018, <https://doi.org/10.1088/1748-9326/ab8032>.
- Sánchez-Benítez, A., R. García-Herrera, D. Barriopedro, P. M. Sousa, and R. M. Trigo, 2018: June 2017: The earliest European summer mega-heatwave of reanalysis period. *Geophys. Res. Lett.*, **45**, 1955–1962, <https://doi.org/10.1002/2018GL077253>.
- Shen, C., J. Zha, J. Wu, D. Zhao, C. Azorin-Molina, W. Fan, and Y. Yu, 2021a: Does CRA-40 outperform other reanalysis products in evaluating near-surface wind speed changes over China. *Atmos. Res.*, **266**, 105948, <https://doi.org/10.1016/j.atmosres.2021.105948>.
- , —, —, and —, 2021b: Centennial-scale variability of terrestrial near-surface wind speed over China from reanalysis. *J. Climate*, **34**, 5829–5846, <https://doi.org/10.1175/JCLI-D-20-0436.1>.
- , —, D. Zhao, J. Wu, W. Fan, M. Yang, and Z. Li, 2021c: Estimating centennial-scale changes in global terrestrial near-surface wind speed based on CMIP6 GCMs. *Environ. Res. Lett.*, **16**, 084039, <https://doi.org/10.1088/1748-9326/ac1378>.
- Song, F., T. Zhou, and Y. Qian, 2014: Response of East Asian summer monsoon to natural and anthropogenic forcings in

- the 17 latest CMIP5 models. *Geophys. Res. Lett.*, **41**, 596–603, <https://doi.org/10.1002/2013GL058705>.
- Song, P., and T. Zhou, 2014: The climatology and interannual variability of East Asian summer monsoon in CMIP5 coupled models: Does air–sea coupling improve the simulations. *J. Climate*, **27**, 8761–8777, <https://doi.org/10.1175/JCLI-D-14-00396.1>.
- Storn, R., and K. Price, 1997: Differential evolution—A simple and efficient heuristic for global optimization over continuous spaces. *J. Global Optim.*, **11**, 341–359, <https://doi.org/10.1023/A:1008202821328>.
- Stott, P. A., 2003: Attribution of regional-scale temperature changes to anthropogenic and natural causes. *Geophys. Res. Lett.*, **30**, 1728, <https://doi.org/10.1029/2003GL017324>.
- Sui, C., P. H. Chung, and T. Li, 2007: Interannual and interdecadal variability of the summertime western North Pacific subtropical high. *Geophys. Res. Lett.*, **34**, L11701, <https://doi.org/10.1029/2006GL029204>.
- Sun, J., H. Wang, and W. Yuan, 2008: Decadal variations of the relationship between the summer North Atlantic Oscillation and middle East Asian air temperature. *J. Geophys. Res.*, **113**, D15107, <https://doi.org/10.1029/2007JD009626>.
- Sun, Y., X. Zhang, F. W. Zwiers, L. Song, H. Wan, T. Hu, H. Yin, and G. Ren, 2014: Rapid increase in the risk of extreme summer heat in Eastern China. *Nat. Climate Change*, **4**, 1082–1085, <https://doi.org/10.1038/nclimate2410>.
- , —, G. Ren, F. W. Zwiers, and T. Hu, 2016: Contribution of urbanization to warming in China. *Nat. Climate Change*, **6**, 706–709, <https://doi.org/10.1038/nclimate2956>.
- Tang, Q., X. Zhang, and J. A. Francis, 2014: Extreme summer weather in northern mid-latitudes linked to a vanishing cryosphere. *Nat. Climate Change*, **4**, 45–50, <https://doi.org/10.1038/nclimate2065>.
- Thompson, G., and T. Eidhammer, 2014: A study of aerosol impacts on clouds and precipitation development in a large winter cyclone. *J. Atmos. Sci.*, **71**, 3636–3658, <https://doi.org/10.1175/JAS-D-13-0305.1>.
- Tokarska, K. B., M. B. Stolpe, S. Sippel, E. M. Fischer, C. J. Smith, F. Lehner, and R. Knutti, 2020: Past warming trend constrains future warming in CMIP models. *Sci. Adv.*, **6**, eaaz9549, <https://doi.org/10.1126/sciadv.aaz9549>.
- Trenberth, K. E., and D. P. Stepaniak, 2001: Indices of El Niño evolution. *J. Climate*, **14**, 1697–1701, [https://doi.org/10.1175/1520-0442\(2001\)014<1697:LIOENO>2.0.CO;2](https://doi.org/10.1175/1520-0442(2001)014<1697:LIOENO>2.0.CO;2).
- Ukkola, A. M., M. G. De Kauwe, M. L. Roderick, G. Abramowitz, and A. J. Pitman, 2020: Robust future changes in meteorological drought in CMIP6 projections despite uncertainty in precipitation. *Geophys. Res. Lett.*, **47**, e2020GL087820, <https://doi.org/10.1029/2020GL087820>.
- Uppala, S. M., and Coauthors, 2005: The ERA-40 re-analysis. *Quart. J. Roy. Meteor. Soc.*, **131**, 2961–3012, <https://doi.org/10.1256/qj.04.176>.
- Verdon, D., and S. W. Franks, 2006: Long-term behaviour of ENSO: Interactions with the PDO over the past 400 years inferred from paleoclimate records. *Geophys. Res. Lett.*, **33**, L06712, <https://doi.org/10.1029/2005GL025052>.
- Wallace, J. M., and D. S. Gutzler, 1981: Teleconnections in the geopotential height field during the Northern Hemisphere winter. *Mon. Wea. Rev.*, **109**, 784–812, [https://doi.org/10.1175/1520-0493\(1981\)109<0784:TITGHF>2.0.CO;2](https://doi.org/10.1175/1520-0493(1981)109<0784:TITGHF>2.0.CO;2).
- Wang, B., L. Ho, Y. Zhang, and M. Lu, 2004: Definition of South China Sea monsoon onset and commencement of the East Asia summer monsoon. *J. Climate*, **17**, 699–710, <https://doi.org/10.1175/2932.1>.
- Wang, C., and D. B. Enfield, 2001: The tropical Western Hemisphere warm pool. *Geophys. Res. Lett.*, **28**, 1635–1638, <https://doi.org/10.1029/2000GL011763>.
- Wang, Y., F. Ren, and X. Zhang, 2014: Spatial and temporal variations of regional high temperature events in China. *Int. J. Climatol.*, **34**, 3054–3065, <https://doi.org/10.1002/joc.3893>.
- Woollings, T., M. Lockwood, G. Masato, C. Bell, and L. Gray, 2010: Enhanced signature of solar variability in Eurasian winter climate. *Geophys. Res. Lett.*, **37**, L20805, <https://doi.org/10.1029/2010GL044601>.
- Wu, C. R., 2013: Interannual modulation of the Pacific decadal oscillation (PDO) on the low-latitude western North Pacific. *Prog. Oceanogr.*, **110**, 49–58, <https://doi.org/10.1016/j.pocean.2012.12.001>.
- Wu, J., J. Zha, and D. Zhao, 2016: Estimating the impact of the changes in land use and cover on the surface wind speed over the East China Plain during the period 1980–2011. *Climate Dyn.*, **46**, 847–863, <https://doi.org/10.1007/s00382-015-2616-z>.
- , —, —, and Q. Yang, 2018a: Changes of wind speed at different heights over Eastern China during 1980–2011. *Int. J. Climatol.*, **38**, 4476–4495, <https://doi.org/10.1002/joc.5681>.
- , —, —, and —, 2018b: Changes in terrestrial near-surface wind speed and their possible causes: An overview. *Climate Dyn.*, **51**, 2039–2078, <https://doi.org/10.1007/s00382-017-3997-y>.
- , Z. Han, Y. Xu, B. Zhou, and X. Gao, 2020: Changes in extreme climate events in China under 1.5°C–4°C global warming targets: Projections using an ensemble of regional climate model simulations. *J. Geophys. Res. Atmos.*, **125**, e2019JD031057, <https://doi.org/10.1029/2019JD031057>.
- Xu, Y., X. Gao, Y. Shen, C. Xu, Y. Shi, and F. Giorgi, 2009: A daily temperature dataset over China and its application in validating a RCM simulation. *Adv. Atmos. Sci.*, **26**, 763–772, <https://doi.org/10.1007/s00376-009-9029-z>.
- Xu, Z., and Z.-L. Yang, 2015: A new dynamical downscaling approach with GCM bias corrections and spectral nudging. *J. Geophys. Res. Atmos.*, **120**, 3063–3084, <https://doi.org/10.1002/2014JD022958>.
- You, J., M. Jian, S. Gao, and J. Cai, 2021: Interdecadal change of the winter–spring tropospheric temperature over Asia and its impact on the South China sea summer monsoon onset. *Front. Earth Sci.*, **8**, 599447, <https://doi.org/10.3389/feart.2020.599447>.
- You, Q., K. Fraedrich, G. Ren, N. Pepin, and S. Kang, 2013: Variability of temperature in the Tibetan Plateau based on homogenized surface stations and reanalysis data. *Int. J. Climatol.*, **33**, 1337–1347, <https://doi.org/10.1002/joc.3512>.
- Yuan, C., T. Tozuka, T. Miyasaka, and T. Yamagata, 2008: Respective influences of IOD and ENSO on Tibetan Plateau snow cover in early winter. *Climate Dyn.*, **33**, 509–520, <https://doi.org/10.1007/s00382-008-0495-2>.
- Zeng, Z. Z., and Coauthors, 2019: A reversal in global terrestrial stilling and its implications for wind energy production. *Nat. Climate Change*, **9**, 979–985, <https://doi.org/10.1038/s41558-019-0622-6>.
- Zha, J., J. Wu, and D. Zhao, 2016: Changes of probabilities in different wind grades induced by land use and cover change in Eastern China Plain during 1980–2011. *Atmos. Sci. Lett.*, **17**, 264–269, <https://doi.org/10.1002/asl.653>.

- , —, and —, 2017: Effects of land use and cover change on the near-surface wind speed over China in the last 30 years. *Prog. Phys. Geogr.*, **41**, 46–67, <https://doi.org/10.1177/0309133316663097>.
- , D. Zhao, J. Wu, and P. Zhang, 2019: Numerical simulation of the effects of land use and cover change on the near-surface wind speed over eastern China. *Climate Dyn.*, **53**, 1783–1803, <https://doi.org/10.1007/s00382-019-04737-w>.
- , J. Wu, D. Zhao, and W. Fan, 2020: Future projections of the near-surface wind speed over eastern China based on CMIP5 datasets. *Climate Dyn.*, **54**, 2362–2361, <https://doi.org/10.1007/s00382-020-05118-4>.
- , and Coauthors, 2021a: Projected changes in global terrestrial near-surface wind speed in 1.5°C–4.0°C global warming levels. *Environ. Res. Lett.*, **16**, 114016, <https://doi.org/10.1088/1748-9326/ac2fdd>.
- , C. Shen, D. Zhao, J. Wu, and W. Fan, 2021b: Slowdown and reversal of terrestrial near-surface wind speed and its future changes over eastern China. *Environ. Res. Lett.*, **16**, 034028, <https://doi.org/10.1088/1748-9326/abe2cd>.
- Zhao, D., J. Zha, and J. Wu, 2018: Comparisons of urban-related warming for Shenzhen and Guangzhou. *Atmos. Oceanic Sci. Lett.*, **11**, 330–337, <https://doi.org/10.1080/16742834.2018.1486681>.
- , —, and —, 2020: Changes in daily and cumulative volumetric rainfall at various intensity levels due to urban surface expansion over China. *Tellus*, **72A** (1), 1–21, <https://doi.org/10.1080/16000870.2020.1745532>.
- , —, and —, 2021: Changes in rainfall of different intensities due to urbanization-induced land-use changes in Shenzhen, China. *Climate Dyn.*, **56**, 2509–2530, <https://doi.org/10.1007/s00382-020-05601-y>.
- Zhu, J., H. Liao, and J. Li, 2012: Increases in aerosol concentrations over eastern China due to the decadal-scale weakening of the East Asian summer monsoon. *Geophys. Res. Lett.*, **39**, L09809, <https://doi.org/10.1029/2012GL051428>.